Bioactive Materials 45 (2025) 301–321

Contents lists available at ScienceDirect

Bioactive Materials

journal homepage: www.keaipublishing.com/en/journals/bioactive-materials

An ATP-activated spatiotemporally controlled hydrogel prodrug system for treating multidrug-resistant bacteria-infected pressure ulcers

Xiaoliang Qi [a], Yajing Xiang [b], Ying Li [c], Jiajia Wang [c], Yuxi Chen [b], Yulong Lan [c], Jinsong Liu [b], Jianliang Shen [a,c,*]

[a] National Engineering Research Center of Ophthalmology and Optometry, Eye Hospital, Wenzhou Medical University, Wenzhou, Zhejiang, 325027, China
[b] School & Hospital of Stomatology, Wenzhou Medical University, Wenzhou, Zhejiang, 325027, China
[c] Zhejiang Engineering Research Center for Tissue Repair Materials, Wenzhou Institute, University of Chinese Academy of Sciences, Wenzhou, Zhejiang, 325001, China

ARTICLE INFO

Keywords:
Prodrug systems
Adenosine triphosphate response
Hydrogels
Multidrug-resistant bacterial infection
Pressure ulcers

ABSTRACT

Adenosine triphosphate (ATP)-activated prodrug approaches demonstrate potential in antibacterial uses. However, their efficacy frequently faces obstacles due to uncontrolled premature activation and spatiotemporal distribution differences under physiological circumstances. Herein, we present an endogenous ATP-activated prodrug system (termed ISD3) consisting of nanoparticles (indole-3-acetic acid/zeolitic imidazolate framework-8@polydopamine@platinum, IZPP) embedded in a silk fibroin-based hydrogel, aimed at treating multidrug-resistant (MDR) bacteria-infected pressure ulcers. Initially, an ultraviolet-triggered adhesive ISD3 barrier is formed over the pressure ulcer wound by a simple local injection. Subsequently, the bacteria-secreted ATP prompts the degradation of IZPP, allowing the loaded IAA prodrug and nanozyme to encounter spatiotemporally on a single carrier, thereby efficiently generating reactive oxygen species (ROS). Exposure to 808 nm near-infrared light enhances the catalytic reaction speed, boosting ROS levels for stronger antibacterial action. Once optimal antibacterial action is reached, ISD3 switches to a dormant state, halting any further ROS production. Moreover, the bioactive components in ISD3 can exert anti-inflammatory functions, aiding in pressure ulcer recovery. Overall, our research introduces a hydrogel prodrug strategy activated by bacterial endogenous ATP, which precisely manages ROS generation and accelerates the recovery of MDR bacteria-infected pressure ulcers.

1. Introduction

Pressure ulcers, often known as decubitus ulcers or bedsores, commonly occur as skin injuries in individuals who spend prolonged periods confined to beds or wheelchairs. These wounds typically arise from sustained mechanical friction and pressure, leading to ischemic damage to the skin and tissues beneath [1]. Groups at high risk for these injuries encompass the elderly, individuals with diabetes, patients receiving intensive care, and those with limited mobility or loss of sensation [2]. Studies in long-term care facilities reveal a variation in the prevalence of pressure ulcers, ranging from 3 % to 31 %, with differences observed in different countries [3]. Not only do these sores negatively impact the quality of life and mental health of patients, but they also contribute to considerable economic costs [4]. Within the United States, nearly 3 million people are afflicted by pressure ulcers, and the yearly expenses for treating these conditions surpass $26 billion [5,6]. Extreme instances of pressure ulcers may result in secondary bacterial infections, acute pain in the affected area, numbness in limbs, tissue death, and various complications, including blood poisoning, low levels of albumin, bone infections, and decay of the femoral head [7]. Presently, antibiotics stand as the primary treatment method for bacterial infections found in pressure sores [8]. However, the prevalent employment of antibiotics has contributed to the emergence of bacteria resistant to multiple drugs, including methicillin-resistant *Staphylococcus aureus* [9]. Such resistance diminishes the efficacy of existing medications and elevates the likelihood of harmful drug interactions [10]. Highlighting the critical need for new therapeutic approaches to combat infections caused by these MDR bacteria is crucial, particularly

Peer review under responsibility of KeAi Communications Co., Ltd.
* Corresponding author. National Engineering Research Center of Ophthalmology and Optometry, Eye Hospital, Wenzhou Medical University, Wenzhou, Zhejiang, 325027, China.
E-mail addresses: shenjl@wiucas.ac.cn, sjl1@wmu.edu.cn (J. Shen).

https://doi.org/10.1016/j.bioactmat.2024.11.029
Received 8 October 2024; Received in revised form 5 November 2024; Accepted 20 November 2024

regarding pressure ulcers in medical environments.

In recent times, antibacterial tactics relying on ROS have surfaced as a highly promising method for treating wounds infected by bacteria [11,12]. These techniques boast non-specific action and notable efficiency, showing formidable inhibitory impacts on MDR bacteria while not fostering antibiotic resistance [13]. Present approaches utilizing ROS for antibacterial purposes encompass photodynamic therapy, chemodynamic therapy, and sonodynamic therapy [14]. ROS predominantly arise from highly reactive areas on the surfaces of materials excited by light. These reactive species act as intermediaries in the redox reactions involving photo-induced electrons/holes with O_2 and H_2O throughout the catalytic process [15]. Their high reactivity leads to cellular damage due to an imbalance between ROS and the antioxidant mechanisms in biomolecules [16]. Efficiently produced through 'one-pot' synthesis methods for effective antibacterial activity, the continued presence of ROS in wounds can aggravate inflammatory responses [17]. Such prolonged inflammation impedes the progression of the wound healing process into later stages, thereby obstructing optimal wound repair [18]. Therefore, alongside leveraging the antimicrobial effects of ROS systems, precise control over ROS release is crucial to prevent exacerbation of inflammatory responses in the wound. Achieving this balance is key to facilitating the repair of MDR bacteria-infected pressure ulcer wounds.

Currently, researchers have discovered the ability to regulate the controlled discharge of ROS through either time-based or spatial manipulation of the ROS mechanism. Prodrugs, which are compounds transformed enzymatically or chemically into their active parent medications at precise moments and sites, provide a potential strategy for accurate ROS release [19]. Prodrugs, generally non-toxic, often present benefits, including enhanced targeting and absorption of drugs, prolonged retention, and diminished side effects relative to their original drug forms. Indole-3-acetic acid (IAA), a naturally occurring prodrug, distinguishes itself among various prodrugs. With the involvement of

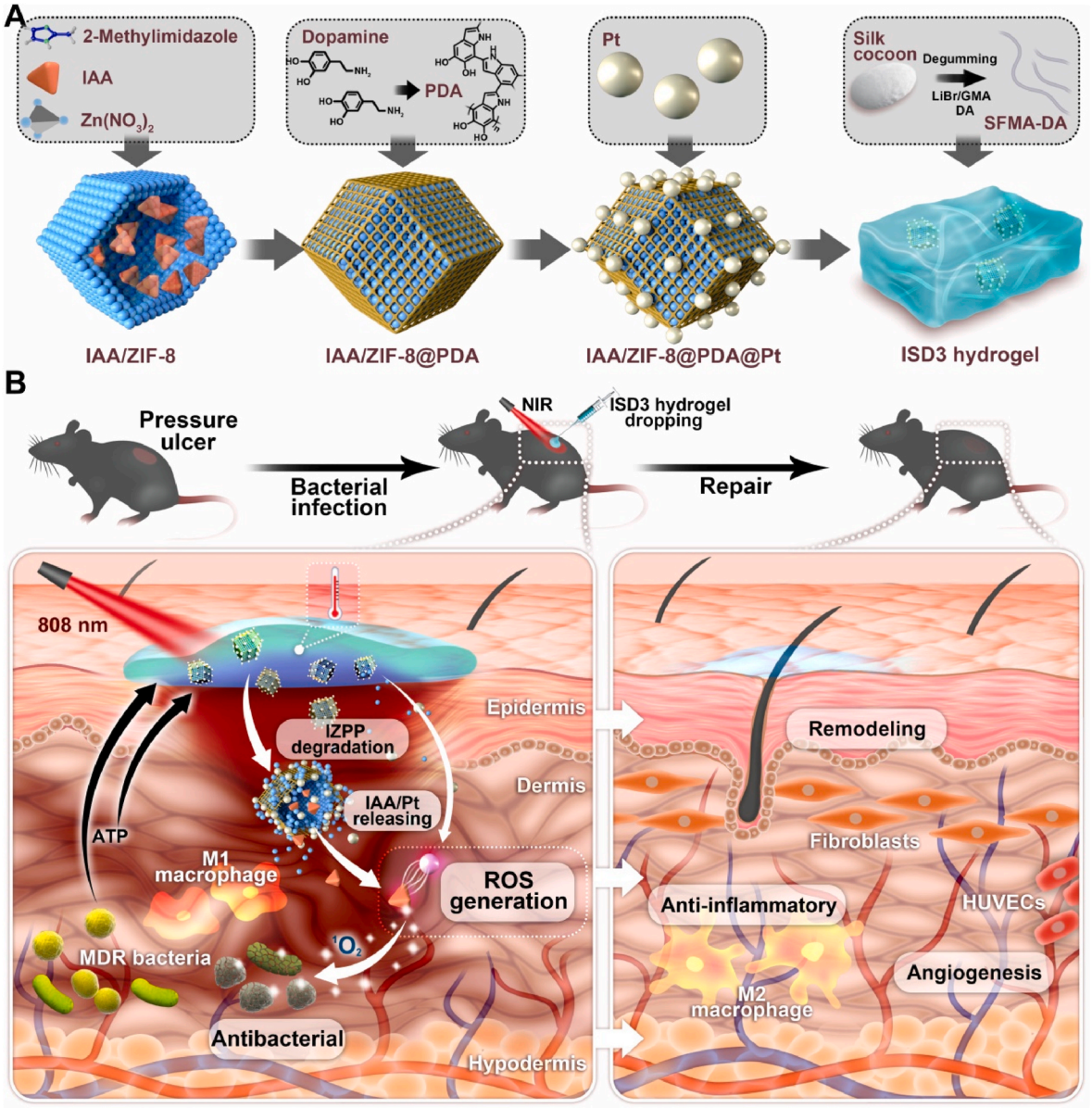

Scheme 1. Illustrative diagram depicting the fabrication and application of the ISD3 hydrogel prodrug system for treating MDR bacteria-infected pressure ulcers. (A) Outlining ISD3's formulation steps. (B) Pathological stages pre (left) and post (right) therapy: subsequent to ISD3 injection at the lesion, the released IZPP underwent degradation through bacterial intrinsic ATP. Boosted by NIR illumination, the released IAA prodrug and the PP nanozyme on the IZPP surface converge spatiotemporally, efficiently generating ROS. Sequentially, this eradicated MDR bacteria and facilitated the pressure ulcer's progression from an inflammatory condition to a reparative phase, culminating in successful wound healing.

peroxidases such as horseradish peroxidase, IAA oxidizes to generate ROS [20]. However, standalone prodrug systems cannot remain at wound sites for prolonged treatment. Hence, a strategy that can sustainably anchor the drug system at the wound site is required. Wound dressings could effectively address this challenge. Researchers have developed various types of wound dressings for therapeutic applications, including porous foams, biocompatible membranes, nanofiber membranes, and functional hydrogels. Among these, hydrogels are notable for their superior biocompatibility and capacity to replicate the extracellular matrix's three-dimensional network structure [21]. Moreover, as moist dressings, hydrogels help to maintain wound moisture, thereby accelerating wound healing [22].

In this study, we propose a strategy for controlled ROS generation using an inorganic-organic hybrid prodrug system. To validate this concept, we designed a hydrogel scaffold (Scheme 1) composed of nanosystem (IAA@zeolitic imidazolate framework-8@polydopamine@platinum, IAA/ZIF-8@PDA@Pt, IZPP) and a hydrogel matrix (dopamine-modified methacrylated silk fibroin, SFMA-DA). Avoiding premature activation of the prodrug (IAA) is critical, so we first utilized the biocompatible and biodegradable zeolitic imidazolate framework-8 (ZIF-8) carrier for the in situ loading of the IAA. Following the encapsulation of IAA in ZIF-8, we applied a polydopamine (PDA) coating to its exterior, which acted as a foundation for Pt nanoparticle deposition. Our intention was for the PDA/Pt (PP) outer layer to exhibit peroxidase-like characteristics, aiding in the catalysis of the liberated IAA. The engineered IZPP system not only facilitates the co-transportation of IAA and PP nanozyme within a single carrier but also physically isolates the pre-loaded IAA from the PP nanozyme to prevent premature activation of IAA and subsequent ROS generation. The IZPP is further encapsulated in a SFMA-DA hydrogel to enhance its dispersibility and stability. SFMA-DA serves a dual function: on the one hand, it captures bacteria through physical interactions, localizing the bacteria-secreted adenosine triphosphate (ATP) and thus intensifying the interaction between PP nanoparticles and IAA for ROS release; on the other hand, it can act as a scaffold for cell proliferation and tissue remodeling. When IZPP/SFMA-DA (abbreviated as ISD3) is applied to the MDR bacteria-infected pressure ulcer regions, bacteria-secreted ATP can trigger the opening of the ZIF-8 structure, allowing the released IAA to encounter PP on the IZPP surface in a single-carrier spatiotemporally precise manner, thereby efficiently generating ROS. Simultaneously, exposure to 808 nm near-infrared radiation enhances the catalytic reaction rate, yielding a higher concentration of ROS for effective antibacterial action. Once efficient antibacterial activity is achieved, the hybrid system transitions to a "dormant" state, ceasing the production of excessive ROS. Additionally, the functional groups (such as polyphenols) within the ISD3 can scavenge inflammatory factors in chronic wounds, which is beneficial for wound repair. In summary, we establish an inorganic-organic hybrid system triggered by bacteria-derived endogenous ATP, effectively enabling on-demand regulation of ROS release and facilitating the accelerated healing of MDR bacteria-infected pressure ulcers.

2. Experimental section

2.1. Materials

Methanol, 1-vinylimidazole, lithium bromide, and ammonium acetate were provided by Macklin (Shanghai, China). N-(3-dimethylaminopropyl)-N′-ethylcarbodiimide hydrochloride (EDC), 3-indoleacetic acid (IAA), 2-methylimidazole, N-hydroxysuccinimide (NHS), adenosine triphosphate (ATP), horseradish peroxidase (HRP), 2-(N-morpholino) ethanesulfonic acid hydrate (MES), potassium tetrachloroplatinate (II), lithium phenyl(2,4,6-trimethylbenzoyl) phosphate salt (LAP), nitro blue tetrazolium chloride (NBT), phenazine methosulfate, vitamin C, nicotinamide adenine dinucleotide, 2-phenyl-4,4,5,5-tetramethylimidazoline-1-oxyl 3-oxide (PTIO), tris (hydroxymethyl) aminomethane, perchloric acid, ferric chloride, sodium carbonate, and glycidyl methacrylate were supplied by Aladdin (Wenzhou, China). Dopamine hydrochloride, deuterium oxide (D_2O) and zinc acetate dihydrate [Zn $(CH_3COO)_2{\cdot}2H_2O$] were provided by Energy Chemical (Wenzhou, China). Cell Counting Kit (CCK)-8 and 2′,7′-dichlorofluorescein diacetate (DCFH-DA) were obtained from Beyotime (Nanjing, China). Calcein acetoxymethyl ester (calcein-AM), streptozotocin, and propidium iodide (PI) were procured from Yeasen (Shanghai, China). A bacterial viability kit comprising PI and SYTO9 was obtained from Thermo Fisher (L7012, Waltham, USA). Gibco (Grand Island, USA) provided Dulbecco's modified Eagle's medium (DMEM), fetal bovine serum, phosphate-buffered saline (PBS) and penicillin-streptomycin. Tryptone Soya Broth and Luria-Bertani Broth came from Hopebiol (Shanghai, China). 1,1-Diphenyl-2-picrylhydrazyl (DPPH) was provided by Innochem (Wenzhou, China). Local suppliers provided all other reagents, which were utilized directly as received, without additional purification.

2.2. Fabrication of IAA/ZIF-8@polydopamine (IZP) nanoparticles

Nanoparticles of IAA/ZIF-8 (IZ) were created using a single-step synthesis technique [23]. Initially, a solution was created by dissolving 74.8 mg of Zn $(CH_3COO)_2{\cdot}2H_2O$ in 2.5 mL of double distilled water (DDW). In a separate procedure, 224 mg of 2-methylimidazole and 30 mg of IAA were combined in another 2.5 mL of DDW and then homogenized using ultrasonic mixing for even dispersion. The two prepared solutions were then blended. The resultant mixture underwent stirring at ambient temperature for 2 h, followed by a 16-h aging period. Post-reaction, the resulting precipitate was washed alternately using ethanol and DDW three times. Ultimately, the cleansed precipitate was subjected to vacuum drying for an entire day, resulting in the production of IZ nanoparticles suitable for further applications. Following the synthesis, the yield was 199.5 mg of IZ nanoparticles. Regarding the mass distribution, IAA constituted 10.98 wt% of IZ, with 199.5 mg of these nanoparticles encompassing 21.9 mg of IAA. Utilizing the traditional colorimetric Salkowski method, our study revealed that IZ exhibited significant encapsulation (with an IAA encapsulation rate reaching 73.3 %, Fig. S1) and minimal leakage (below 4.8 % of the encapsulated IAA released from IZ for 90 h in PBS, Fig. S2).

To create the PDA layer, 10 mg of IZ nanoparticles were first dissolved in 24 mL of tris (hydroxymethyl) aminomethane buffer solution, maintaining a pH of 8.5 [24]. The solution was then stirred magnetically at 37 °C for 20 min. Subsequently, 5 mg of dopamine hydrochloride was added to the mixture, followed by continuous magnetic stirring for an additional 6 h. After the reaction, the formed material was thoroughly rinsed multiple times, alternating between ethanol and DDW. Following the cleansing process, the substance was subjected to vacuum drying over 24 h, yielding IZP nanoparticles prepared for ensuing applications. The IZP nanosystem demonstrated IAA degradation triggered by ATP, as shown by an increasing rate of IAA release corresponding to higher ATP concentrations (Fig. S3).

2.3. Fabrication of IZPP nanoparticles

For the synthesis of IZPP nanoparticles, an initial step involved dissolving 10 mg of IZP in 20 mL of DDW, which was then transferred to a round-bottom flask. Concurrently, in a different vessel, 30 mg of potassium chloroplatinite was dissolved in 0.61 mL of DDW and underwent ultrasonic mixing to achieve uniform dispersion [25]. Following this, the potassium chloroplatinite solution was combined with the IZP solution in the flask. The reaction of these mixed solutions proceeded at 80 °C for 24 h. Following the chemical reaction, the resultant precipitate was washed in an alternating manner with ethanol and DDW, completing this at least three times. After the washing process, the material underwent 24 h of vacuum drying, yielding IZPP nanoparticles suitable for subsequent applications.

2.4. Synthesis of methacrylated silk fibroin (SFMA)

To isolate silk fibroin (SF), cocoon shells were treated in a sodium carbonate solution with a concentration of 0.02 M for 1 h to eliminate sericin. Following that, 2 g of the degummed SF was combined with 10 mL of a 9.3 M concentration lithium bromide solution. The obtained mixture was heated to 60 °C and combined with 350 mM of glycidyl methacrylate. Agitation of the blend was carried out at 300 rpm for 3 h. To finalize the process, the resulting SFMA compound was dialyzed in DDW over five days and preserved at a temperature of 4 °C for future use.

2.5. Synthesis of dopamine-modified SFMA (SFMA-DA)

The SFMA was chemically linked to dopamine hydrochloride through a reaction that utilized EDC and NHS as catalysts [26]. To start, 3.0 g of SFMA was mixed in 300 mL of degassed MES buffer (100 mM, pH 4.5) and maintained at a temperature of 37 °C. Subsequently, EDC and NHS, weighing 1725.3 mg and 1035.9 mg, respectively, were introduced into the solution. Following 20 min of stirring, a solution of dopamine hydrochloride (1706.7 mg) in 9 mL of MES buffer (100 mM, pH 3.3) was incorporated into the blend. The combined solutions were allowed to undergo a reaction at 37 °C in a dark environment, with agitation at 100 rpm, for 24 h. Post-reaction, the synthesized compound was then transferred to a dialysis membrane featuring a molecular weight cutoff of 12 kDa. It was first dialyzed in a 1 mM HCl solution for two days, then in DDW for an additional day. The material was lyophilized to yield the final SFMA-DA compound, suitable for further applications.

2.6. Fabrication of IZPP/SFMA-DA (ISD) hydrogels

Different IZPP nanoparticle concentrations were introduced into a 10 % SFMA-DA solution at ambient temperature to create a range of hydrogels. To achieve homogeneity, the mixture underwent further blending. Following that, a photoinitiator known as LAP was added at a concentration of 0.4 %. Exposure to ultraviolet light for 1 min led to the formation of a stable ISD hydrogel. Four distinct hydrogel formulations were developed in the experiment, each containing IZPP dosages of 0, 0.5, 1, and 2 mg/mL. These hydrogels were designated as ISD1, ISD2, ISD3, and ISD4 for identification purposes. Meanwhile, the pure SFMA hydrogel was named ISD0.

2.7. Physicochemical characterization

Fourier transform infrared (FTIR) analysis was performed on the samples using a Bruker Spectrometer (Germany), which came equipped with an attenuated total reflectance accessory from ThermoFisher. Spectra collection occurred in the wavenumber spectrum of 4000 to 400 cm^{-1}, employing a resolution of 4 cm^{-1}. For proton nuclear magnetic resonance (^1H NMR) research, samples were prepared with D_2O as the solvent and analyzed employing a Quantum-I 400 MHz device (China). The spectra from ^1H NMR were gathered and examined through Mestrenova software. Ultraviolet–visible–near-infrared (UV–VIS–NIR) spectra of fabricated samples were performed using a Cary5000 spectrophotometer (Agilent, USA) under ambient temperature [27]. The fabricated nanomaterials underwent examination with a JEM-1230 transmission electron microscopy (TEM) (Jeol, Japan) functioning at 100 kV. Before the TEM analysis, a suspension in water with the designed nanomaterials was spread onto copper grids coated with a carbon film. The microstructure of the hydrogels was analyzed employing a SU8010 scanning electron microscope (SEM, Hitachi, Japan). Preparation for SEM involved lyophilizing the hydrogel samples. At first, the hydrogels were thoroughly frozen at −80 °C for 24 h. Subsequently, the frozen specimens were moved to a freeze dryer, where they remained for 48 h to achieve thorough dehydration. Following the drying process, the hydrogels were sectioned to expose their cross-sections by rapidly immersing them in liquid nitrogen. In order to enhance conductivity and facilitate imaging, the samples received a coating of gold nanoparticles (each less than 20 nm thick) for around 30 s in a vacuum environment. Energy dispersive X-ray (S4800 FEG, Hitachi, Japan) was used to obtain cross-sectional elemental profiles.

2.8. ATP response of IZPP

For exogenous ATP response, after adding 5 mM ATP to a 1 mg/mL IZPP solution and incubating at 37 °C for 30 min, the structure of IZPP was observed using SEM.

For bacteria-secreted ATP response, IZPP (1 mg/mL) was combined with bacterial cultures containing 1×10^7 [colony-forming units (CFU)/mL)] of either methicillin-resistant *Staphylococcus aureus* (MRSA). Subsequent to various treatments, the mixture comprising IZPP and the bacteria was filtered employing a 0.45 μm membrane (Millex-HV, USA). The resultant filtrate was then freeze-dried, and the sample obtained was examined using SEM. The antimicrobial effect of IZPP nanoparticles was also evaluated at different concentrations and irradiation with NIR light. We utilized the plate counting technique to assess MRSA bacterial suspensions subjected to various treatments. These samples were distributed onto agar culture plates and incubated at 37 °C for 24 h. Following incubation, we counted the bacterial colonies.

2.9. Swelling

The swelling behavior of the ISD hydrogels in a wet state was assessed as follows: ISD hydrogels were positioned in a sealed tube with PBS (pH = 7.4) at 37 °C, mimicking wound exudate environments. Periodically, these hydrogels were extracted from the tube, and their mass was recorded post removal of surplus PBS using filter paper. This method was repeated until the hydrogel weight stabilized [28]. Subsequently, swelling ratios of the hydrogels were determined using the formula Swelling Ratio = $(W_a - W_b)/W_b$, where W_a is the hydrogel weight after a designated swelling duration, and W_b is the hydrogel weight prior to swelling.

2.10. Water retention

To evaluate the water retention capabilities of the hydrogels, cylindrical samples (8 mm thick, 10 mm diameter) were exposed to conditions with 37 °C temperature and 30 % relative humidity. The hydrogels' weight was measured periodically over 12 h using a digital scale. The water retention ratio at any given time was determined using the formula: Water Retention (%) = $W_i/W_0 \times 100$ %, where W_i signifies the ISD hydrogel's weight at the time i and W_0 denotes the hydrogel's initial weight.

2.11. Hydrogel degradation behaviors

The degradation characteristics of the ISD hydrogels in a wet state were assessed after reaching swelling equilibrium. The hydrogels were situated in a sealed tube with PBS (pH = 7.4) at 37 °C, mimicking wound environments. They were periodically taken out of the tube, and their mass was ascertained after blotting away excess PBS with filter paper. This procedure was repeated until complete biodegradation of the hydrogels occurred. To calculate the biodegradation ratios, the remaining mass of the hydrogels was used, applying the formula: Degradation (%) = $(W_c - W_d)/W_c \times 100$ %, where W_d is the hydrogel's weight post a certain biodegradation period, and W_c is the hydrogel's weight when it reached swelling equilibrium.

2.12. Rheological performance

The rheological profiles of the hydrogels (ISD1, ISD2, ISD3, and

ISD4) were evaluated employing a stress-controlled TA DHR-2 rheometer (USA) [29]. The hydrogels, measuring 1 mm in height and 25 mm in diameter, were fabricated specifically for the subsequent measurement modes: (a) A series of strain sweep experiments were performed at 25 °C on the prepared samples to identify the linear viscoelastic range. The oscillation strain ranged from 0.1 % to 1000 %. (b) Tests sweeping frequency were carried out at 25 °C to explore the connection between frequency and modulus (storage modulus G′ and loss modulus G″), with frequency adjustments ranging from 0.1 to 100 Hz. (c) To ascertain the gelation time of the ISD hydrogels, dynamic oscillatory time sweep tests were executed with a fixed frequency of 0.1 Hz and a strain of 1 %. (d) Dynamic stepwise strain amplitude tests were performed to assess the hydrogels' self-healing properties. The oscillatory strain alternated between large (400 %) and small (1 %) values with short intervals. (e) Shear-thinning measurements were conducted to assess the viscosity behavior of the ISD hydrogels. The shear rate varied from 0.1 to 60 1/s.

2.13. IAA release assay

Initially, to determine the standard curve of IAA, we utilized the Salkowski reagent, comprising a mixture of ferric chloride (0.5 M) and 35 % perchloric acid. The Salkowski colorimetric assay involved mixing varying IAA concentrations (ranging from 0 to 3 mg/mL) with 150 μL of the Salkowski reagent, allowing a reaction time of 30 min at ambient temperature. To maintain a consistent total volume of 300 μL for the assay, 10 mM PBS buffer (pH 7.4) was added as needed. Following this, IZPP nanoparticles or ISD hydrogels were measured and submerged in 20 mL of PBS containing ATP at various concentrations. At predetermined intervals, 2 mL of the solution was drawn out and replaced with an identical volume of new PBS buffer. The released IAA during this process was then combined with the Salkowski reagent. We measured the absorbance of this mixture at 529 nm using UV–VIS–NIR spectroscopy.

2.14. ROS scavenging activity

To begin with, the capability of ISD3 hydrogel to counteract oxidants was assessed using a PTIO (oxygen radicals) radical scavenging test. Commonly, a solution of 4 mL PTIO in water (200 μg/mL) was concocted and introduced into various tubes, each holding 50 mg of ISD3, DDW, and vitamin C (at a concentration of 8 mg/mL). Following a 6-h co-incubation at 37 °C, the absorbance of the clear liquid above the settled material at 559 nm was measured using a UV–VIS–NIR spectrophotometer.

Secondly, the DPPH (nitrogen radicals) radical scavenging assay was conducted to evaluate the antioxidant capacity of the hydrogel. A DPPH/ethanol solution (0.1 mM) was prepared. Hydrogel specimens were submerged in DPPH solution and incubated at 37 °C in darkness for 30 min. Afterward, the mixture was moved to a cuvette, and a spectrophotometer was used to measure each sample's absorbance at 517 nm. The formula used to compute the DPPH radical scavenging percentage is as follows: Scavenging Rate (%) = $(1 - A_b/A_n) \times 100$ %, in which A_n stands for the initial absorbance of the DPPH solution, while A_b refers to the absorbance observed in the mixture after incubating the DPPH with the test sample for 30 min.

Finally, the ability of the hydrogel to neutralize superoxide radicals ($O_2^{\bullet-}$) underwent evaluation using the NBT assay. The ISD3 hydrogel specimen was immersed in a mixture consisting of NBT, nicotinamide adenine dinucleotide, and phenazine methosulfate, all dissolved in a PBS solution. Post a 5 min incubation at 37 °C, the mixture's absorbance was gauged at 560 nm. To ascertain the hydrogel's effectiveness in neutralizing $O_2^{\bullet-}$, the formula Scavenging Rate (%) = $(1 - A_d/A_g) \times 100$ % was applied. Here, A_g stands for the absorbance of the blank control group, while A_d indicates the absorbance of the group that underwent treatment with the hydrogel.

2.15. ROS production ability

To assess the catalytic effectiveness of samples in the oxidation of 3,3′,5,5′-tetramethylbenzidine (TMB, Sigma, Shanghai, China), we introduced 40 μg/mL of IZPP nanoparticles (or 100 mg/mL ISD3 hydrogel) into a 5 mM ATP solution to create a mixture, to which we then added 0.5 mM TMB dissolved in DMSO. This mixture was incubated for 2 h. Subsequently, 200 μL of this mixture was withdrawn and deposited into a clean 96-well plate to analyze oxidation through UV–VIS–NIR spectroscopy, specifically noting the 652 nm peak to evaluate the catalytic impact on the oxidized TMB (oxTMB). After a 2-h room temperature incubation, another 200 μL was sampled from the mixture and placed in a fresh 96-well plate for the same UV–VIS–NIR spectroscopic analysis to further confirm the catalytic activity on oxTMB.

Additionally, the efficacy of various synthesized nanomaterials in generating ROS was evaluated through flow cytometry. RS1 and macrophages (RAW 264.7 cells) were cultivated in cell culture disks and allowed to incubate overnight. Subsequently, nanomaterials, DCFH-DA, and ATP were introduced to the culture medium. Post a 20 min incubation period, the cells were separated employing trypsin digestion and washed thrice with PBS. Finally, the fluorescence intensity emitted by the RS1 and RAW 264.7 cells was quantitatively ascertained using a flow cytometer.

2.16. Analysis of released IAA products catalyzed by IZPP

High-performance liquid chromatography-mass spectrometry (HPLC-MS) (1290 Infinity II + 6135MS, Agilent, USA) was utilized for the product analysis of IZPP. HRP (1 mg/mL) or IZPP (1 mg/mL) combined with liberated IAA (0.2 mg/mL) were amalgamated and left to incubate overnight. Subsequently, the resulting supernatant was collected and subjected to reverse-phase HPLC using a C18 Columbus column (Poroshell 120 EC-C18, Agilent, USA). Gradient elution was executed with a methanol/water mixture (50:50, v/v, containing 7.5 mM ammonium acetate) at a flow rate of 0.5 mL/min.

2.17. Cell experiments

2.17.1. CCK-8 assay

Firstly, the CCK-8 method was employed to evaluate the toxicity of developed ISD hydrogels on macrophages and RS1 cells. Dry gel samples were first sterilized with a 70 % ethanol solution and then rinsed three times with a sterile PBS solution. Subsequently, the samples were immersed in a DMEM culture medium with serum for 24 h. All procedures were conducted in a laminar flow hood.

After seeding 6×10^3 RAW 264.7 or RS1 cells into each of the 96 wells, the plate was incubated at 37 °C for 24 h. The medium from the 96-well plate was then removed, and hydrogel extract was introduced into each well. Subsequent cultivation periods for the cells were set for 1, 3, and 5 days. After these intervals, each well received a fresh medium infused with 10 % CCK-8, followed by an additional 4-h incubation. Subsequently, the plate was positioned in a microplate reader to assess the optical density at 450 nm. Cells that were not exposed to the hydrogel extract served as the negative control [30]. The formula used to calculate cell viability was: Cell Viability (%) = $A_2/A_1 \times 100$ %, wherein A_2 corresponds to the absorbance of the treated group and A_1 to the absorbance of the control cohort.

2.17.2. Cell live/dead staining

To assess cell viability visually, the live/dead cell staining method was employed for determining cell vitality [31]. Cultures of macrophages and RS1 cells were grown in cell culture disks, maintaining a density of 6×10^4 cells per well, followed by an incubation of 12 h. Next, the hydrogel leachate was introduced into these dishes. Following a three-day culture period, staining of both dead and live cells was carried

out as per the guidelines of the calcein-AM/PI staining kit. For imaging purposes, a Nikon confocal microscope from Japan was utilized.

2.17.3. Intracellular antioxidant performance

Initially, the CCK-8 technique was employed to measure the ROS scavenging capabilities of the material at a cellular scale. Cultures of RAW 264.7 and RS1 cells were allocated to a 96-well plate, each well containing a seeding density of 6×10^3 cells. Post a 24-h incubation time, the original culture medium was removed and replaced with a fresh one. Subsequently, hydrogen peroxide (H_2O_2) solutions, which had been treated with different hydrogels, were added to the culture medium. The macrophages and RS1 cells were further incubated in a darkened cell culture incubator at 37 °C for 4 h. Subsequently, their viability was assessed by employing the CCK-8 kit.

Next, following the treatment of different groups, cellular ROS levels were quantified using DCFH-DA, a fluorescent probe specific for ROS detection. Initially, the macrophages and RS1 cells were cultured in 24-well culture dishes, undergoing an incubation period of 24 h. After discarding the cell culture medium, the adherent cells underwent treatment with a medium containing H_2O_2 solutions that had been exposed to various hydrogels for 6 h. In accordance with the prescribed protocol, a measured amount of DCFH-DA was added, after which the cells' morphology was observed under a confocal microscope.

Lastly, the performance of hydrogels in clearing intracellular ROS was assessed using flow cytometry. Macrophages and RS1 cells cultured in 6-well plates underwent the previously described treatment process. After a 20 min incubation employing the fluorescent probe DCFH-DA, these cells were dissociated via trypsin digestion and then washed three times with PBS. The fluorescence intensity emitted by the cells was then quantified using a flow cytometer.

2.17.4. Cell scratching assay

First, sterilized thin hydrogel sheets were positioned at the base of a 6-well plate. Well-developed RS1 cells were then dispersed on the hydrogel's surface. Upon reaching 90 % confluence, the hydrogel's surface was delicately scraped with a 100 μL pipette tip and then rinsed with PBS to eliminate any detached cells. The moment immediately following the scraping was marked as 0 h, and cell morphology was captured and documented using a microscope. The cells were then placed in a cell culture incubator for durations of 12 and 24 h. Cell morphology was again observed and recorded at each of these time points under a microscope.

2.17.5. In vitro angiogenesis

Typically, each well of a 96-well plate was coated evenly with 10 μL of matrigel and then incubated for 1 h at 37 °C to allow for solidification. Following this, human umbilical vein endothelial cells (HUVECs) were cultured atop the matrigel layer at a seeding density of 1×10^4 cells in each well. Once the cells had adhered to the underlying substrate, an extract of the hydrogel was introduced. Following a 12-h incubation period, staining was performed using a calcein-AM staining kit, as per the manufacturer's guidelines. Microscopic examination was employed to observe and document the angiogenic response.

2.18. Hemocompatibility assay

To evaluate the hemocompatibility of ISD hydrogels, rat blood samples were first centrifuged at 2000 rpm for a 10 min duration to collect red blood cells. These cells were washed thrice with PBS and subsequently diluted to attain a 5 % (v/v) final concentration. Then, 0.5 mL of this cell suspension was combined with 50 mg of ISD samples inside a 1.5 mL tube. Post incubation of the tubes at 37 °C for 1 h, subsequent centrifugation at 2000 rpm for 10 min took place. Following this, the resulting supernatant was distributed into a 96-well plate, with 100 μL allocated to every well. Absorbance readings were then taken at 545 nm using an Agilent (USA) Cary5000 spectrophotometer. In this evaluation, DDW functioned as the positive control, while PBS was utilized as the negative control.

2.19. Antibacterial assay

The antibacterial properties of the ISD3 were investigated using MRSA. We prepared a blend of 5 mL liquid bacterial culture medium with 50 μL MRSA suspension at a concentration of 1×10^7 CFU/mL. The mixture was incubated for 14 h at 37 °C with shaking at 130 rpm. Subsequently, the bacterial suspension was further diluted 1:1000 (v/v) for further experiments. We introduced 100 mg of the sample (either hydrogel or PBS) into 1 mL of bacterial suspension. Following a designated incubation duration, 40 μL of the bacterial solution was distributed uniformly across agar plates. These agar plates were subsequently left to incubate overnight at 37 °C. Bacterial growth was monitored by counting colonies and taking photographic records.

Following treatments across various groups, bacterial suspensions were gathered and rinsed thrice using PBS. Thereafter, the bacteria underwent fixation in glutaraldehyde (2.5 %) at 4 °C for an overnight period. Following a series of ethanol dehydration steps (25 %, 50 %, 75 %, and 100 % ethanol gradients), the bacterial morphology was observed using SEM.

The viability of bacteria with intact or damaged membranes was assessed using the L7012 bacterial viability assay kit containing PI and SYTO9. Post-treatment with different ISD hydrogel bacterial suspensions underwent staining as per the guidelines of the assay kit. After the staining process, the bacteria were cleansed thrice with PBS and then visualized using laser scanning confocal microscopy.

2.20. In vivo pressure ulcer wound healing

Animal experiments were performed adhering to the guidelines of the Animal Ethics Committee at Wenzhou Medical University, approved under number xmsq2022-0238. Male six-week-old C57 mice provided by Beijing Vital River (China) were used in the study. To create pressure ulcer injuries, neodymium magnets were applied to the dorsal skin of these mice. First, the mice's fur was eliminated from their backs with Veet shaving. The layers of dorsal skin—epidermis, dermis, subcutaneous fat, and loose connective tissue, omitting muscles—were meticulously elevated and positioned between two circular neodymium magnets, with each magnet being 12 mm in diameter and 5 mm in height. Next, the mice were subjected to a pressure ulcer regimen comprising 12-h ischemia cycles followed by 12-h perfusion cycles, repeated for three full cycles.

Every mouse manifested two separate circular areas of purpura or ulcers, divided by a strip of unblemished skin. Following this, a bacterial solution of MRSA (10 μL, at a concentration of 1×10^7 CFU/mL) was directly dripped onto the ulcer wound area. MRSA-infected mice were then arbitrarily divided into five different sets, each containing six mice: one for the control using PBS, a second as a positive control with 3M Tegaderm film, a third receiving ISD1 treatment, a fourth for treatment with ISD3, and a fifth for treatment with ISD3 combined with laser exposure (1.0 W/cm^2 for 1.5 min). Each set designated for hydrogel treatment received a 100 μL sample of the corresponding hydrogel. Documentation and photography were conducted on days 0, 3, 7, and 14 after an intervention to record the condition of the injured area. Afterward, the mice were euthanized humanely, and tissue samples from the wounds were harvested at the predefined times for additional study.

2.21. In vivo photothermal performance

Mice were arbitrarily and uniformly allocated into three distinct groups, each consisting of three mice: PBS, ISD1, and ISD3. The wounds treated with PBS and hydrogels underwent exposure to 808 nm NIR radiation at an intensity of 1 W/cm^2 for 180 s. Thermal infrared pictures of these areas were acquired with a specialized camera.

2.22. Repair mechanism analysis

Following euthanasia, the mouse skin surrounding the wound was excised for histologic examination. The collected tissues and organs were fixed in a 4 % paraformaldehyde solution. After 24 h of fixation, the tissues were processed for hematoxylin and eosin (H&E), tumor necrosis factor-alpha (TNF-α), Masson, platelet endothelial cell adhesion molecule-1 (CD31), CD86 (M1 marker), and CD206 (M2 marker) staining to generate histological slides. Confocal microscopy was used to observe and capture images of the stained slides, and image analysis software (ImageJ) was employed to detect fluorescence in the sections, evaluating parameters such as anti-inflammatory response, collagen deposition, and wound healing efficiency. Concurrently, key organs from the mice, including the heart, liver, spleen, kidney, and lung, were gathered and underwent H&E staining to assess biosafety.

2.23. Transcriptome sequencing

Total RNA underwent extraction via the Trizol reagent provided by Invitrogen in California, following the guidelines laid out by the manufacturer. Subsequent evaluation of RNA purity and measurement was carried out with a NanoDrop 2000 device from Thermo Fisher Scientific (USA). For investigating RNA integrity, the Agilent 2100 Bioanalyzer from Agilent Technologies (California, USA) was employed. Subsequently, library construction was conducted employing the VAHTS Universal V6 RNA-seq Library Prep Kit in accordance with the manufacturer's provided instructions.

2.24. Statistical analysis

The macroscopic and histological findings were examined by three experts who were unaware of the group assignments. Statistical analyses were presented as the means ± standard deviation (SD), utilizing GraphPad Prism 8 software. For assessing statistical significance, the unpaired Student's t-test and either one-way or two-way ANOVA with Tukey's post hoc test were employed, depending on the situation. All experiment replications were biological. The significance levels were established at the following thresholds: NS (not significant, $P > 0.05$), *$P \leq 0.05$, **$P \leq 0.01$, and ***$P \leq 0.001$.

3. Results and discussion

3.1. Design strategies

In this study, we developed an innovative system using a bacterially activated prodrug, specifically IAA, aimed at treating MDR bacterial infections in pressure ulcer wounds. IAA, a tryptophan metabolite, is a naturally occurring prodrug present in human plasma at micromolar concentrations. Research has shown that humans can withstand IAA doses up to 100 mg/kg without significant adverse effects. Catalyzed by peroxidase, particularly potent HRP, IAA undergoes one-electron oxidation, generating free radical intermediates. These intermediates are effective in triggering apoptosis in both bacteria and cancer cells [19, 32]. However, HRP's natural form has limitations, including low efficiency and vulnerability to inactivation, posing challenges in harsh wound environments characterized by bacterial infections, elevated oxidative stress, and high protease levels. Therefore, our approach involves employing Pt inorganic nanozyme as a replacement for traditional HRP. This interaction with the IAA prodrug creates a ROS-generating system. The PP nanozyme, in contrast to natural HRP, demonstrates enhanced catalytic performance, superior stability, ease of preparation, and cost-effectiveness, making it more suitable for challenging wound environments.

Upon optimizing ROS generation, we acknowledged the non-selectivity of ROS, which harms both bacteria and normal cells at the injury site. Consequently, we explored the feasibility of creating a selectively activated IAA/Pt system for targeted ROS production, aiming to eliminate drug-resistant bacteria while sparing healthy cells. To achieve targeted ROS delivery post IAA and Pt interaction, we loaded IAA prodrug and Pt inside and outside of ZIF-8@PDA and integrated this configuration into a SFMA-DA matrix to extend its effective period. This structure, referred to as ISD3, upon application to the wound area, releases IZPP in the presence of bacteria. The bacteria-secreted ATP disrupts the ZIF-8, triggering IAA release and subsequent ROS formation via interaction with PP nanozyme spatiotemporally, thereby neutralizing the bacteria. Conversely, in proximity to healthy cells, which lack sufficient ATP to break down ZIF-8, IAA remains contained, preventing ROS production and safeguarding the normal cells from damage.

Once we attained targeted bacteria eradication, the physicochemical composition and biological elements of the ISD3 hydrogel, including its porous adsorptive characteristics, polyphenolic groups, and Pt's peroxidase-like activity, enhance wound healing progression from inflammation to repair. This is achieved by adsorbing and neutralizing pathways of inflammatory factors, consequently facilitating the superior quality restoration of pressure ulcer injuries.

3.2. Fabrication and characterization of IZPP nanoparticles

Our objective is to develop a core-shell configuration that facilitates the simultaneous encapsulation of IAA and Pt within the same nanostructure. Firstly, TEM and SEM were employed to inspect the microstructure of the synthesized nanocomposites [IAA/ZIF-8, IAA/ZIF-8@PDA, and IZPP]. Observations from SEM and TEM images (Fig. 1A) revealed that the IAA-loaded ZIF-8 (IAA/ZIF-8) maintains a rhombic dodecahedral form with a smooth exterior, averaging around 245.7 nm, similar in appearance to bare ZIF-8 nanoparticles (Fig. S4). The IAA/ZIF-8@PDA, when coated with PDA, transformed into a spherical-like shape with a PDA layer thickness of about 26.6 nm. The subsequent deposition of Pt nanoparticles (around 9.9 nm) onto IAA/ZIF-8@PDA formed IZPP nanoparticles, which are spherical with a distinct core-shell structure and a consistent diameter near 272.3 nm. TEM elemental mapping revealed a consistent distribution of Pt across IAA/ZIF-8@PDA, confirming the successful attachment of Pt nanoparticles (Fig. 1B). The zeta potential data indicated a weakened negative potential of IZPP compared to IAA/ZIF-8@PDA, which may be due to the polyphenol moiety of PDA used for the reduction of Pt^{2+} (Fig. 1C). Furthermore, the ATP-responsive nature of IZPP nanoparticles was evaluated using SEM. Upon exposure to ATP, significant disintegration of IZPP (white arrows in Fig. 1D) was observed, demonstrating its high sensitivity to ATP. This sensitivity likely stems from ATP's stronger affinity for Zn^{2+} over 2-methylimidazole, leading to the displacement of 2-methylimidazole in the ZIF-8 structure and consequent release of IAA [19].

Next, our analysis focused extensively on the photothermal traits induced by NIR in IZPP nanoparticles. The aim was to ensure that IZPP offers an augmented enzymatic effect through heat while concurrently preventing the tissue harm typically associated with concentrated areas of elevated temperatures. Initially, varying concentrations of these nanoparticles underwent NIR laser exposure (808 nm, 1 W/cm^2). Real-time thermal images (Fig. S5) demonstrated that contrary to phosphate-buffered saline (PBS), the temperature variations in IZPP nanoparticles were notably significant. According to the data in Fig. S6, after a 10 min irradiation period, IZPP nanoparticles at dosages of 2, 1, and 0.5 mg/mL attained temperatures of 65.4, 58.4, and 44.6 °C, respectively. The power density also influenced the photothermal behavior of these nanoparticles, as shown in Fig. S7. Despite experiencing four rounds of heating and cooling, the thermal trends of the nanoparticles remained consistent, signifying robust photothermal stability (Figs. S8 and S9). Furthermore, we calculated the photothermal conversion efficiency (PCE) of IZPP nanoparticles, and these nanoparticles demonstrated a high PCE, reaching up to 63.3 % (Figs. S10 and S11). Given the potential for high temperatures to harm healthy tissues, in our research, we regulated the local temperature induced by NIR to a mild hyperthermia

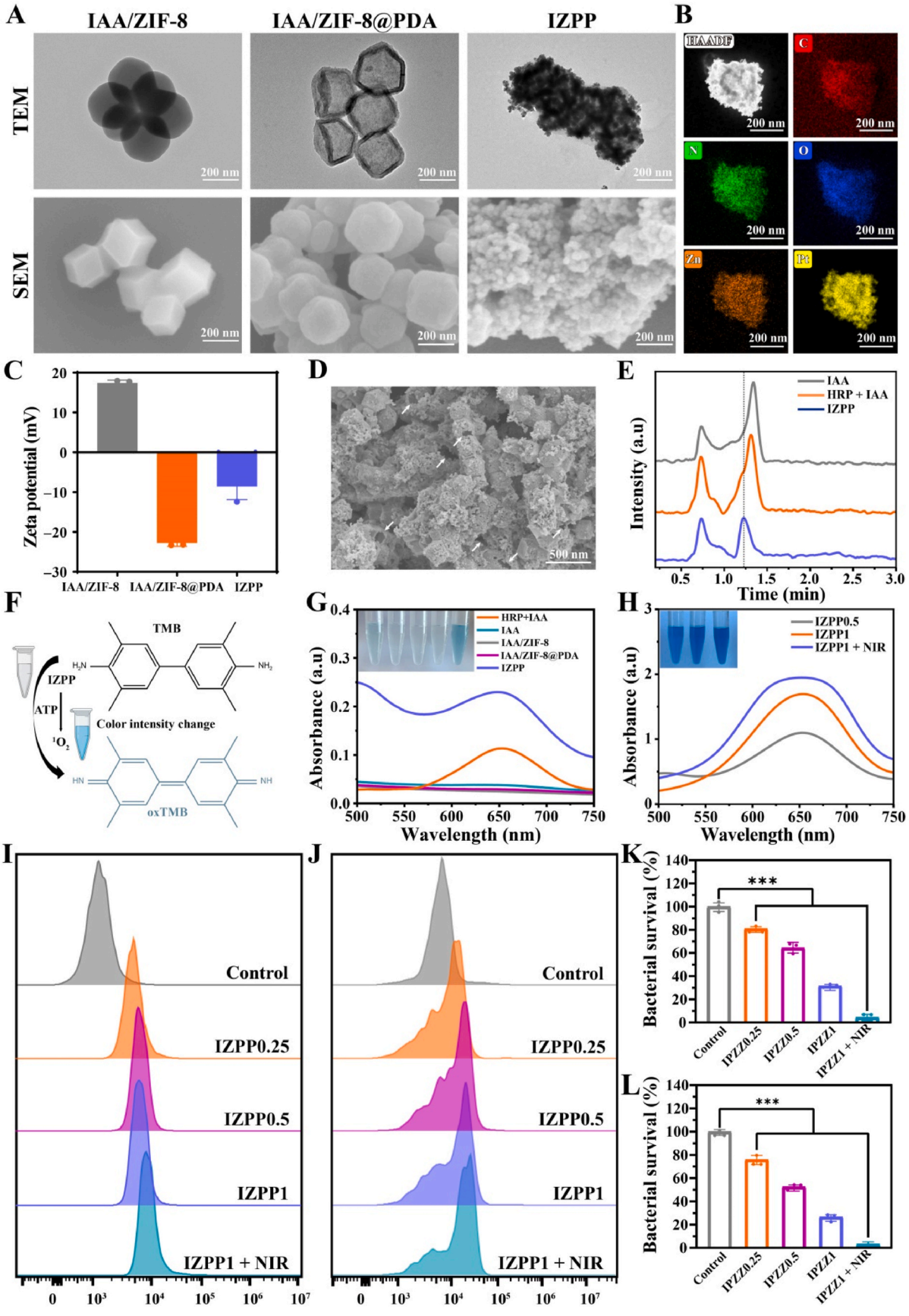

(caption on next page)

Fig. 1. Examining the IZPP nanoparticles' physical, chemical, and biological attributes. (A) TEM and SEM images of IAA/ZIF-8, IAA/ZIF-8@PDA and IZPP. (B) Representative image of IZPP captured through TEM, along with its elemental mapping (HAADF: high-angle annular dark field). (C) Zeta potential of IAA/ZIF-8, IAA/ZIF-8@PDA and IZPP. (D) SEM image of IZPP after 5 mM ATP incubation for 10 min. (E) Chromatographic profile of the reaction's output post-incubation of either HRP or IZPP with IAA. (F) Illustrative schematic showing IZPP's ROS generation via the TMB colorimetric process. (G) UV–VIS–NIR spectral analysis with corresponding images of TMB mixtures reacted with various samples for 15 min in ATP's presence. (H) UV–VIS–NIR spectra of TMB for varying IZPP concentrations with ATP present. (I and J) Flow cytometric characterization of DCFH-DA stained RAW 264.7 (I) and RS1 (J) cells following varied IZPP exposures with ATP. (K and L) Comparative study of antibacterial effects against MRSA (K) and MRPA (L) across different sample groups. Error bars denote mean ± SD (n = 6). *** signifies P < 0.001.

level (<45 °C) [33–35]. Based on the preceding photothermal results, further studies will employ IZPP nanoparticles at a concentration of 1 mg/mL, an irradiation duration of 1.5 min, and a NIR power setting of 1.0 W/cm^2 to guarantee secure and efficient thermal (approximately 42 °C) assisted outcomes.

Following that, we examined if IZPP nanoparticles could catalyze released IAA to produce ROS. First, we used high-performance liquid chromatography-mass spectrometry (HPLC-MS) to demonstrate whether Pt can catalyze IAA oxidation as well as HRP (Fig. 1E). Compared with pure IAA, the HRP/IAA system showed small new peaks. In contrast, the characteristic peaks of IAA of the IZPP system disappeared, and strong new absorption peaks appeared, indicating the depletion of IAA and the generation of new products. Discovery revealed that the ultimate products of IZPP's IAA catalysis were indole-3-aldehyde and indole-3-carbinol. These compounds exhibited relative molecular weights of 145 and 147, matching their respective singly charged ionized forms. Both of these resulting substances matched the outcomes when HRP interacted with IAA. Meanwhile, we used TMB assay to verify whether IAA released from IZPP catalytically oxidized by Pt could also produce ROS (single-linear oxygen species, $^1O_2$) as in the HRP/IAA system. ROS transforms the colorless TMB into a blue oxidized form (oxTMB, $\lambda_{max} = 652$ nm, Fig. 1F). Among the various samples, the IZPP group showed the strongest blue color, indicating that TMB interacted with the most ROS (Fig. 1G). Remarkably, ROS generation is positively correlated with IZPP concentration, as shown in Fig. 1H. Simultaneously, NIR light-induced photothermal effects, stemming from PDA and Pt components known for photothermal conversion, were found to boost IZPP's ROS production capacity. This enhancement likely results from the heightened catalytic performance of Pt enzymes under heat. The dependence of IZPP on concentration and NIR makes it possible for us to provide a controlled release of ROS.

Subsequently, we confirmed the capacity of the IZPP system to produce ROS at the cellular level. We employed the DCFH-DA (2′,7′-dichlorofluorescein diacetate) probe for assessing ROS production in various systems. Results depicted in RAW 264.7 cells (Fig. 1I) and RS1 cells (Figure IJ) indicated that subsequent to introducing a blend of ATP and IZPP to the DCFH solution, a notable green fluorescence was detected, marking ROS production from ATP and IZPP interaction. Moreover, we observed that green fluorescence intensity within cells correlated with the concentration of IZPP. Incrementally adding nanoparticles to the culture medium caused a corresponding increase in cellular green fluorescence intensity. Upon additional NIR stimulation, IZPP (1 mg/mL) demonstrated the most robust green fluorescence, suggesting the highest ROS production level.

In our final phase, we evaluated IZPP's antibacterial effectiveness in vitro. Recognizing that bacteria typically emit ATP as they grow, we refrained from introducing additional ATP in our antibacterial property tests. We selected MRSA (ATCC 43310) and MRPA (ATCC 27853) as test bacteria. When comparing untreated bacteria (blank) with those exposed to IZPP, a clear antibacterial impact was evident. Notably, for MRSA, increasing IZPP concentration in the bacterial mixture from 0 mg/mL to 1 mg/mL led to a reduction in bacterial survival rate from 100 % to 35 %. Upon applying NIR, IZPP showed its most potent bactericidal effect at a concentration of 1 mg/mL, reducing bacterial survival to less than 2.7 % (Fig. 1K). A similar antibacterial trend is reflected in the MRPA (Fig. 1L). These results collectively emphasize the remarkable ability of IZPP to control bactericidal activity mediated by ROS, which is triggered by the bacteria's innate ATP.

3.3. Fabrication and characterization of ISD3 hydrogel

Having confirmed the effectiveness of IZPP nanoparticles, we incorporated these into a hydrogel matrix made of SFMA-DA. A straightforward local injection created an ultraviolet (UV)-activated adhesive barrier, known as ISD3 hydrogel, covering the pressure sore lesion. Following this, the encapsulated IZPP nanoparticles were gradually liberated and stimulated by the surrounding wound microenvironment, executing their designed therapeutic role.

To scrutinize the shifts in functional groups following the ISD3 hydrogel fabrication, both ^{1}H NMR and FTIR spectroscopic methods were employed. A marked transformation in the ^{1}H NMR spectra was observed when comparing SF to its altered form, SFMA. In SFMA's ^{1}H NMR spectrum, resonance peaks for carbon-carbon double bonds were evident at 5.57 and 5.97 ppm [36]. These data confirm the effective incorporation of glycidyl methacrylate into SF. Additionally, the emergence of a methyl group signal at 1.76 ppm corroborated the successful synthesis of SFMA. In a side-by-side evaluation with SFMA, the amino signals in SFMA-DA were intensified, whereas the carboxyl signals were reduced. This shift can be ascribed to the ample amino groups on the dopamine surface, which interact with and diminish the carboxyl groups on SFMA (Fig. 2A and S12). Complementary FTIR data, depicted in Fig. 2B, lend further support to these modifications in signal patterns [37].

Subsequently, an analysis using SEM was conducted to scrutinize the microscopic architecture and surface texture of the freeze-dried ISD hydrogels. As illustrated in Fig. 2C and D, hydrogels ISD1 and ISD3 both displayed a porous, three-dimensional lattice framework, making them well-suited for absorbing wound discharge and promoting cellular proliferation [38]. High-magnification SEM images revealed a smooth interior for ISD1 and a comparatively rough inner texture for ISD3, a feature likely due to the inclusion of IZPP nanoparticles. Notably, the addition of IZPP nanoparticles appeared to alter the hydrogels' average pore dimensions: ISD1 featured an average pore diameter of 54.4 μm, whereas ISD3 had a smaller mean pore size, measuring 40.5 μm.

Following that, the ISD hydrogel dressings were assessed for their swelling and deswelling properties. The water absorption patterns for ISD1 (no encapsulation of IZPP nanoparticles) and ISD3 hydrogels, as shown in the swelling curves (Fig. 2E), exhibited similarities: quick absorption occurred in the first 40 min, succeeded by a slower stabilization beyond 7 h. At equilibrium, ISD1 had a water uptake ratio of 19.7, slightly greater than ISD3's 17.3. This difference indicates enhanced cross-linking in the hydrogels due to the incorporation of IZPP nanoparticles. In terms of moisture retention, ISD hydrogels were oven-dried at 37 °C until their weights stabilized. ISD3 outperformed ISD1 in moisture retention, as illustrated in Fig. 2F. These findings confirm that the synthesized ISD3 hydrogel excels in both water absorption and retention, making it well-suited for promptly absorbing wound discharge and sustaining a favorable moist environment for wound recovery.

Next, the photothermal characteristics of ISD hydrogels were evaluated (Fig. 2G–K). As illustrated in Fig. 2G and H, a more rapid temperature increase in the ISD hydrogels was noted as the IZPP concentration rose. Notably, a concentration of 0.5 mg/mL IZPP led to a temperature surge to 47.3 °C. When IZPP concentrations were further

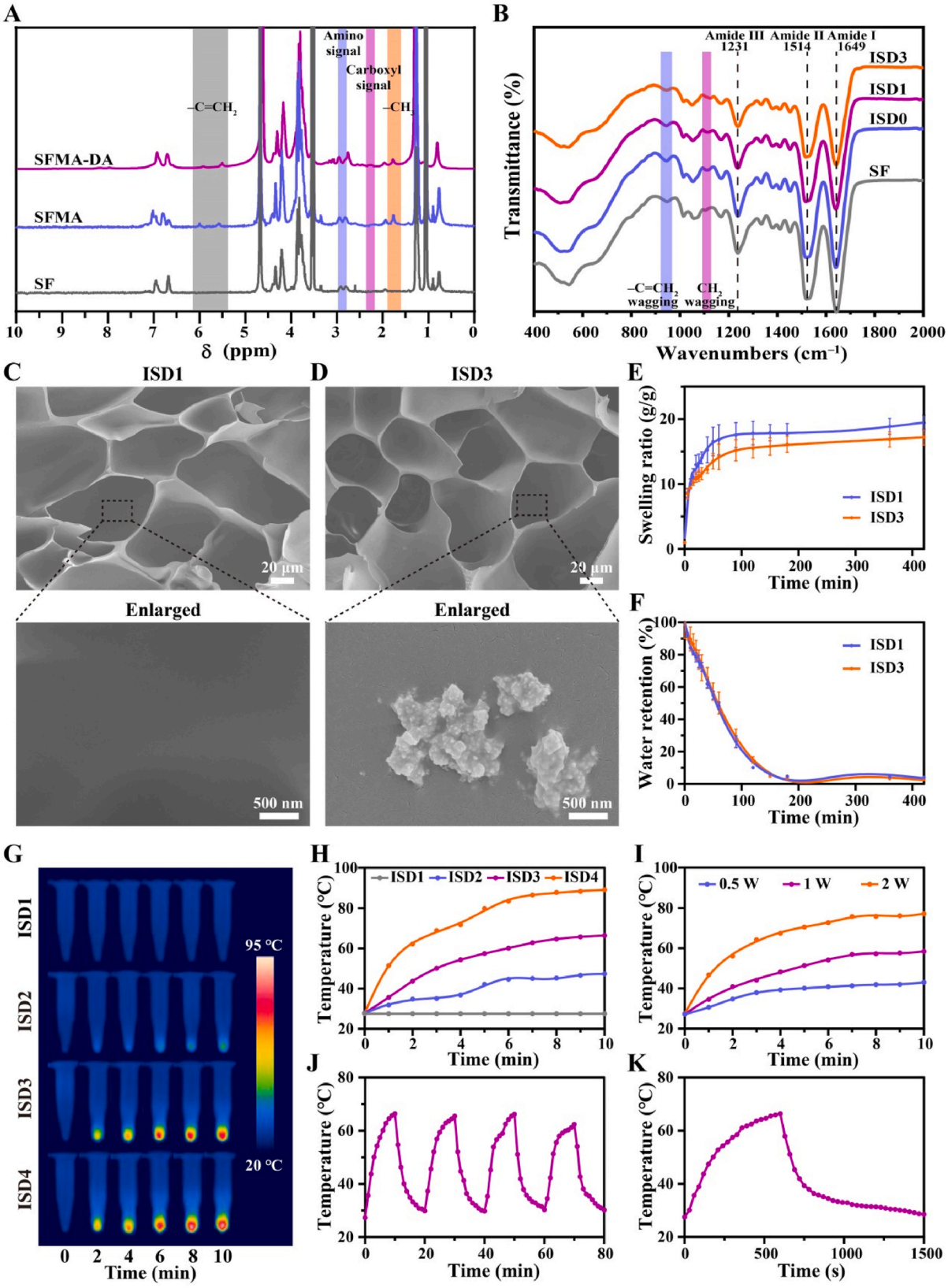

Fig. 2. Evaluation of ISD3 hydrogel's physical and chemical characteristics. (A) ^{1}H NMR spectral data for original SF, SFMA, and SFMA-DA. (B) FTIR spectral profiles for unmodified SF, ISD0, ISD1, and ISD3. (C and D) SEM imagery at multiple magnification levels for ISD1 (F) and ISD3 (G). (E and F) Assessment of swelling (D) and moisture retention (E) capabilities of ISD1 and ISD3. (G) Thermal images of ISD hydrogels post various manipulations. (H) Temperature change patterns associated with assorted hydrogels. (I) Varied NIR exposure conditions and their corresponding impact on ISD3 hydrogel thermal profiles. (J and K) Heat cycling (J) and temperature oscillation (K) graphs for ISD3 under 1 W/cm^2 NIR illumination. Error bars indicate mean ± SD (n = 6).

increased to 1 and 2 mg/mL, corresponding temperatures soared to 66.4 and 89.1 °C. A comparable thermal elevation was observed when laser power density was incrementally raised while keeping the IZPP nanoparticle concentration constant in the hydrogel (Fig. 2I). Thermal imagery captured after 10 min of 808 nm light exposure was in alignment with the observed temperature elevation trends. To evaluate photothermal stability, the hydrogels were allowed to cool down naturally post a 10 min light treatment. Fig. 2J reveals minimal lasting temperature reduction after four cycles of laser activation and deactivation, underscoring the hydrogel's robust photothermal stability. The ISD3 hydrogel's photothermal conversion efficiency, a crucial metric for assessing photothermal attributes, was measured at 54.6 % (Fig. 2K and S13). This data further emphasizes the substantial photothermal capabilities of the engineered ISD3 hydrogel.

3.4. Mechanical and degradation performance of ISD3 hydrogel

In assessing hydrogel dressings, mechanical resilience and adaptability are crucial for conforming to the ever-changing wound microenvironment. To scrutinize the mechanical attributes of ISD hydrogels, a DHR-2 rheometer was employed. Initially, we evaluated how ISD hydrogels transitioned in their state before and after UV light exposure.

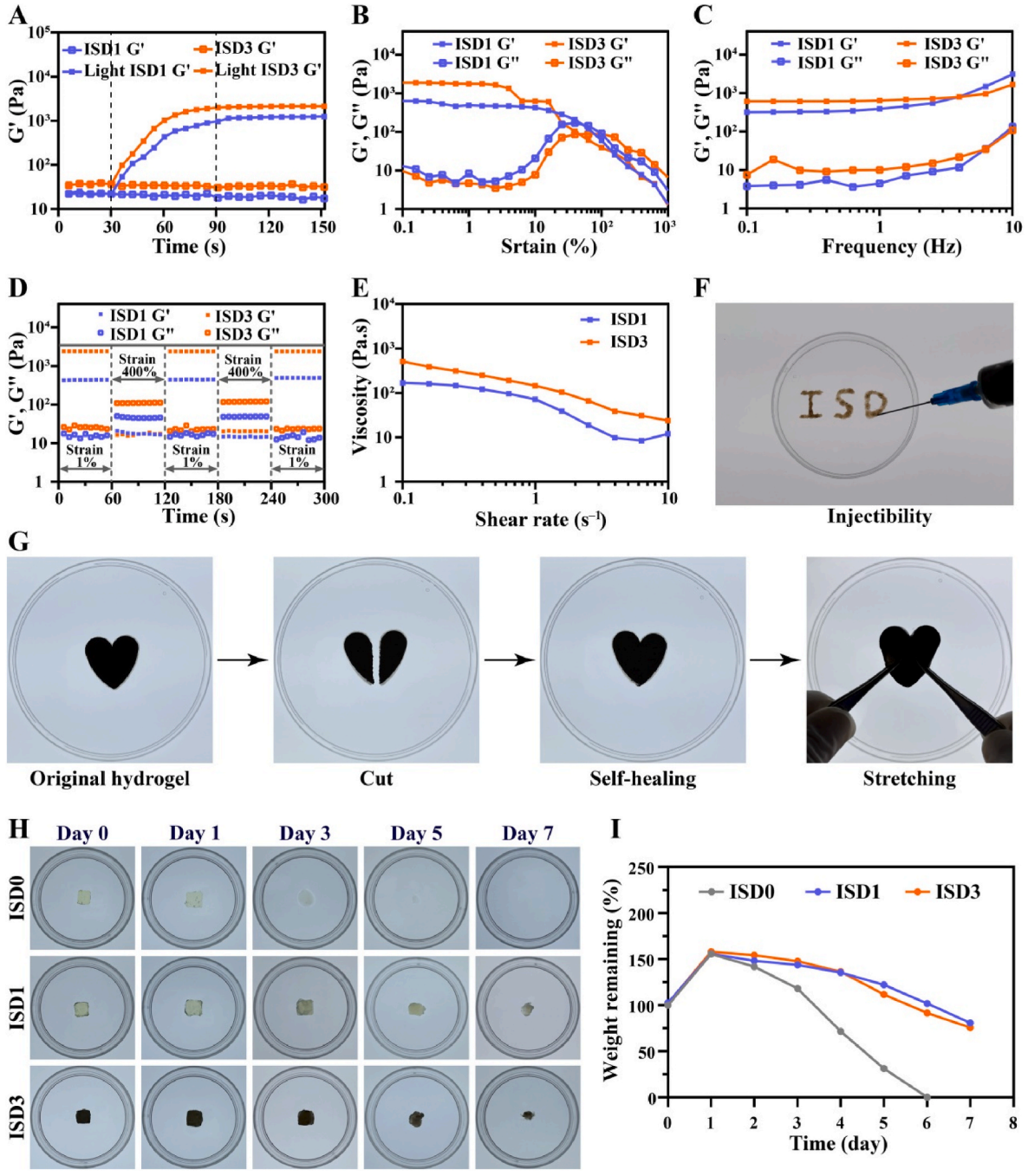

Fig. 3. Mechanical attributes and degradation characteristics of ISD3 hydrogel. (A–E) Rheological assessments of ISD encompassing dynamic strain variations pre and post-UV exposure (A), amplitude analysis (B), oscillation frequency assessment (C), dynamic step-strain evaluation (D), and evaluation of shear-thinning properties (E). (F) Visualizations of ISD3 hydrogel as it has injected onto a plastic surface. (G) Illustrations highlighting the self-mending capabilities of ISD3 hydrogel. (H) Photographic documentation capturing ISD hydrogel degradation at 37 °C in PBS. (I) Residual mass of ISD hydrogels when submerged in PBS at 37 °C.

As evidenced in Fig. 3A, both ISD1 and ISD3 had low storage moduli (G′) prior to UV exposure, indicating a fluidic nature. Within the first minute of UV exposure, a sharp increase in G′ was observed for both hydrogels, followed by stabilization, culminating in a colloidal state [39]. Such behavior allows the hydrogels to bond in situ to irregularly shaped wounds. Subsequently, the hydrogels' linear viscoelastic regions were explored through strain scan experiments. The ISD3 hydrogel's gelation threshold was approximately 30 %, indicating a shift to a liquid state upon the strain surpassing that level (Fig. 3B). Additionally, the rheological characteristics were analyzed over various oscillation frequencies, spanning from 0.1 to 10 Hz (Fig. 3C). Both types of hydrogel demonstrated stable periods where the storage modulus (G′) exceeded the loss modulus (G″), confirming their largely elastic characteristics [40]. To gauge the hydrogels' self-repairing capabilities, dynamic amplitude measurements were conducted (Fig. 3D). To examine the resilience of the hydrogel network, a substantial strain of 400 % was initially imposed, causing disruption. Subsequently, a minimal strain of 1 % was adopted to assess the network's ability to recover. During the high-strain phase, a more substantial drop was observed in G′ compared to G″, revealing a network disruption. Upon reducing the strain to 1 %, both moduli reverted to their initial values, evidencing quick self-recovery. Dynamic sites capable of reversible cross-linking between IZPP and SFMA-DA contribute to the remarkable self-healing properties of ISD3 hydrogel. Lastly, shear testing revealed that the ISD3 hydrogel displayed behavior indicative of shear thinning due to its dynamic physical cross-linking sites, indicating the effective injectability of the material (Fig. 3E) [41].

Furthermore, macroscopic photographs were utilized to explore the ISD3 hydrogels' capabilities for injection and self-repair. Using a 2 mL syringe, the hydrogel was dispensed into a dish and shaped into the letter "ISD" (Fig. 3F), illustrating its effective injectability [42]. After splitting the ISD3 hydrogel into two parts, they autonomously rejoined in a 4-h timeframe without the need for external forces. These rejoined hydrogels closely resembled their original state (Fig. 3G). Based on these observations, ISD hydrogels exhibit impressive mechanical features, such as the ability to be injected and to self-heal, making them highly suitable for treating complex wounds. Conventional wound dressings frequently lack durability and struggle to adhere securely to wound sites [43]. On the other hand, ISD3 hydrogel demonstrated strong adherence to a range of rat tissues, including the heart, liver, spleen, lungs, and kidneys (Fig. S14). Such adhesion lays the foundation for the hydrogel's functionalities in antimicrobial, anti-inflammatory, and wound healing applications [44].

To evaluate the degradation characteristics of ISD hydrogels, these materials were immersed in PBS. We assessed their degradation by both tracking changes in mass and examining their shape over time. As depicted in Fig. 3H, the mass of all three types of ISD hydrogels showed an increase on the first day, a consequence of the swelling behavior. In subsequent days, ISD0 began to fragment into smaller sections. By day 6, ISD0 had almost entirely vanished. In contrast, ISD1 and ISD3 experienced slower rates of degradation, likely due to their enhanced mechanical strength and a greater degree of cross-linking as a result of nanoparticle incorporation (Fig. 3I). Such findings indicate that the synthesized hydrogels are capable of degrading over time, potentially serving essential roles in wound coagulation, inflammation control, and tissue repair without causing further harm [45].

3.5. In vitro biocompatibility of ISD3 hydrogel

Effective use of hydrogels for wound healing is fundamentally rooted in their biological compatibility [46]. We started by assessing the cell compatibility of the engineered ISD3 hydrogel. By employing the CCK-8 tests, the viability of RAW 264.7 and RS1 cells was assessed after they were cultured in extracts from ISD hydrogel over various time intervals. As displayed in Fig. 4A–B, the ISD1 and ISD3 groups sustained over 80 % viable cells compared to normal culture conditions, indicating minimal toxicity for these ISD hydrogels. After a 72-h incubation period, live/-dead cell staining kits were employed on RAW 264.7 and RS1 cells. Calcein-AM colors living cells green, while PI imparts a red hue to dead cells [47]. Green fluorescence levels in ISD3 hydrogel were approximately equivalent to those in the control group, with few dead cells present (Fig. 4C–D).

To delve deeper into the toxicity of designed ISD3 hydrogel on cellular activities under oxidative stress conditions, scratch assays were conducted. A scratch was generated at the base of a 6-well plate filled with RS1 cells using a pipette tip. Subsequently, ISD3 hydrogel leachate was added to observe changes within the scratched area at intervals of 12 and 24 h. Fig. 4E illustrates that cells in both control and ISD3 hydrogel-treated groups maintained their ability to migrate and develop normally over time. The remaining scratch area after 24 h was below 4.9 % of its initial size (Fig. S15), which implies that the ISD3 hydrogel did not hinder regular cellular growth.

Furthermore, HUVECs were employed to estimate the influence of the newly created ISD3 hydrogel on vasculogenesis. Our observations revealed the emergence of polygonal or rounded cell formations on Matrigel's surface, as shown in Fig. 4F [48]. Within 4 h, cells from both the control and hydrogel-treated groups showed a propensity to link up and aggregate. Extending the culture period to 8 h revealed that HUVECs in the control and ISD3 sets connected and constructed a tubular network featuring enhanced blood vessel numbers and greater structural integrity, signifying that ISD3 hydrogel treatment did not affect the vasculogenic capacity of the HUVECs.

We also evaluated the ISD3 hydrogel's blood compatibility through hemolysis tests. Fig. S16 illustrates that the supernatant of the positive control group, which used DDW, turned bright red, signifying the breaking of red blood cells and subsequent hemoglobin release [49]. Conversely, supernatants from both the PBS and hydrogel sets retained a colorless appearance, with a hemolytic rate below 5 %, indicating significant hemocompatibility [50]. Such results collectively imply that the developed ISD3 hydrogel possesses advantageous compatibility with cells and blood, underscoring its potential as a scaffold material for tissue engineering applications.

3.6. In vitro antibacterial and anti-biofilm properties of ISD3 hydrogel

Incomplete wound healing often results from wound infection [51, 52]. To evaluate the antibacterial potential of ISD3 hydrogel, the plate counting technique was utilized to measure its efficacy against MRSA, both with and without 808 nm NIR laser exposure (Fig. 5A). The ISD3 hydrogel formulation showed partial bacterial elimination, achieving a 67.2 % inhibition rate against MRSA (Fig. S17). This hydrogel's bacterial-killing capability correlates strongly with the ATP-activated ROS produced by IAA and Pt. Unsurprisingly, nearly complete bacterial elimination was seen in the ISD3 + NIR group. The bacteria were exposed to a microthermal setting (42 °C) created with NIR (808 nm, 1 W/cm^2, for 1 min), which activated ROS production through PP nanozyme and IAA prodrug, substantially boosting the ISD3 hydrogel's sterilization performance.

To explore the underlying mechanisms of antibacterial action, bacterial morphological alterations were assessed through SEM. As seen in Fig. 5A, MRSA cells in the ISD1 hydrogel group, either with or without 808 nm laser exposure, generally displayed spherical shapes with smooth, intact membranes—similar to untreated MRSA [53]. In contrast, the bacterial forms within the ISD3 hydrogel group, particularly when subjected to NIR activation, exhibited significant distortions, and some even appeared ruptured. These observations affirm that the photothermal effects of NIR activation enhance the bactericidal efficiency of ISD3 hydrogel.

Further scrutiny of bacterial membrane integrity was conducted through live/dead bacterial staining techniques. Interestingly, in both the control and ISD1 hydrogel groups, as well as the ISD1 + NIR group, predominantly green fluorescence was observed, indicating a lack of

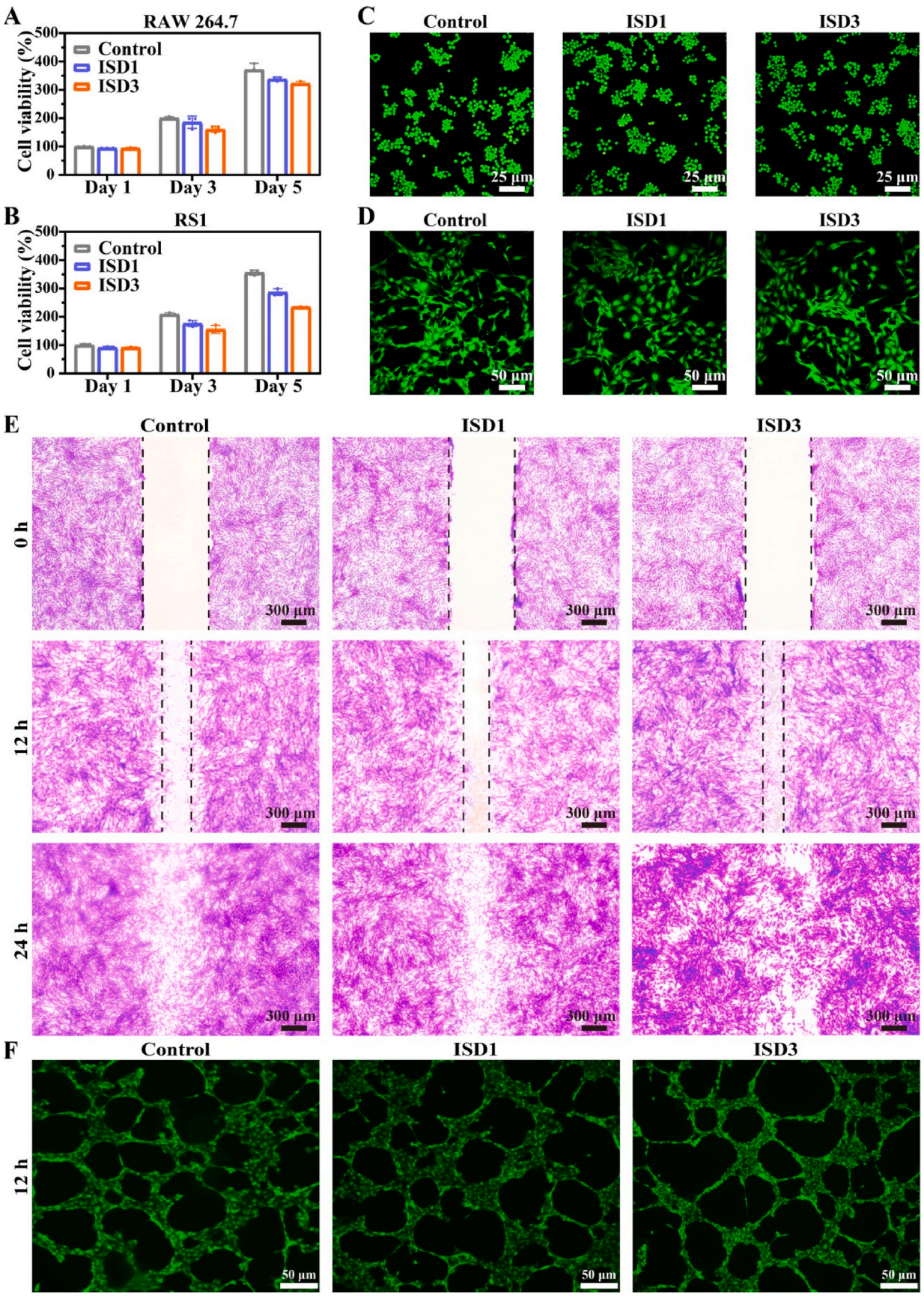

Fig. 4. In vitro biocompatibility of ISD3 hydrogel. (A and B) CCK-8 based toxicity evaluation for RAW 264.7 cells (A) and RS1 cells (B). (C and D) Results from calcein-AM/PI labeling on RAW 264.7 cells (C) and RS1 cells (D) following a 72-h incubation with different treatments. (E) Analysis of RS1 cell movement after creating a scratch at intervals of 0, 12, and 24 h. (F) Pictorial representation of vascular network development in HUVECs following diverse treatment types.

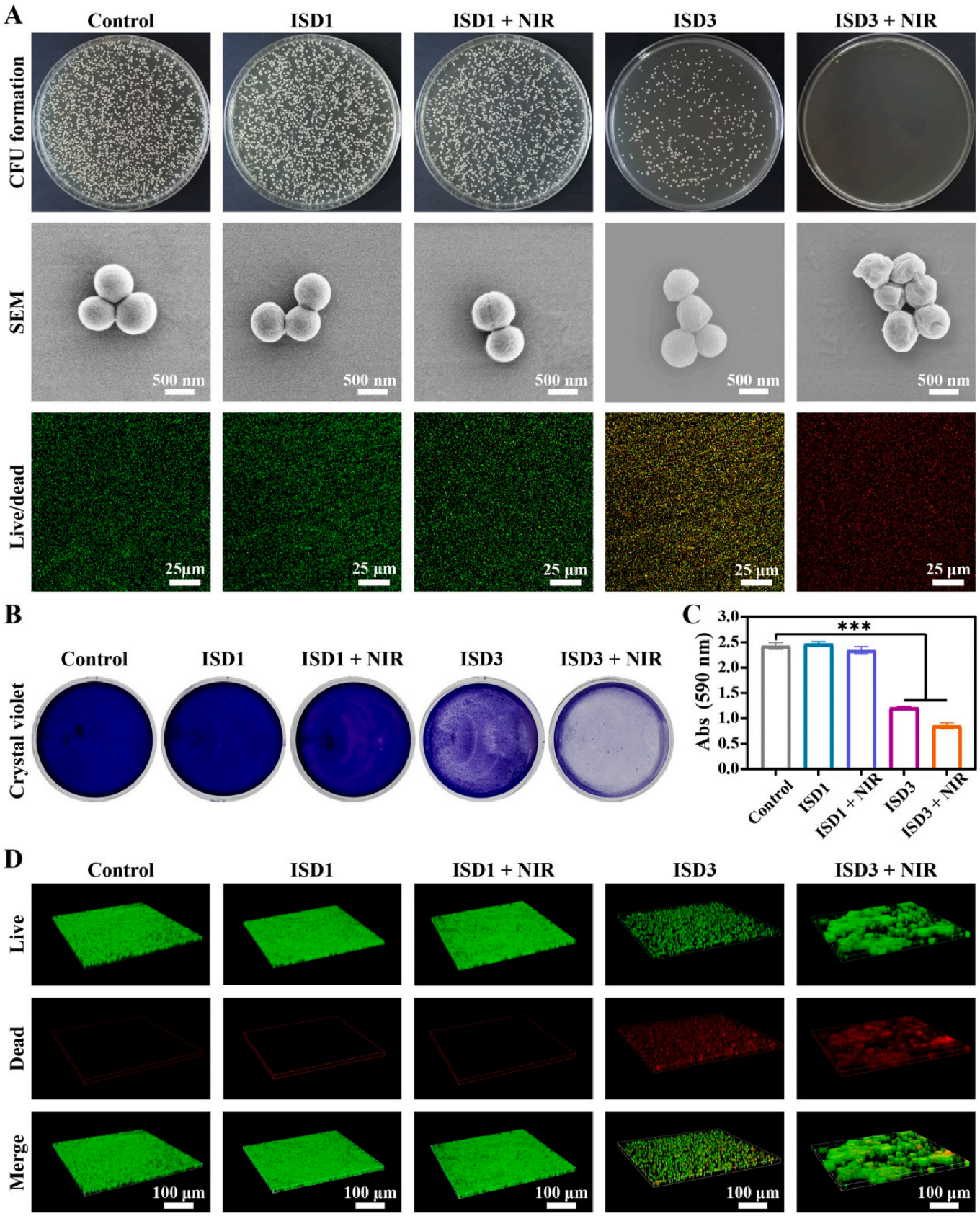

Fig. 5. In vitro evaluation of ISD3 hydrogel's antibacterial and anti-biofilm efficacy. (A) Plate counts, SEM, and live-dead bacterial staining methods used to gauge ISD hydrogel's antibacterial performance against MRSA. (B and C) Crystal violet assays for MRSA biofilms (B) and subsequent measurement of absorbance at 590 nm (C). (D) Three-dimensional confocal laser scanning microscopy visuals of MRSA biofilms post-varied treatments (green fluorescence representing SYTO9-stained MRSA biofilms; red fluorescence denoting PI). Error bars indicate the mean ± SD (n = 6). A significance level of $P < 0.001$ is denoted by ***.

antibacterial activity. In contrast, the ISD3 hydrogel group displayed some red fluorescence, hinting at a bactericidal impact. Most strikingly, the combination of ISD3 and NIR yielded the brightest red fluorescence, as PI could infiltrate the compromised bacterial membrane, resulting in red staining (Fig. S18). Such findings point to the ISD3 hydrogel as an apt candidate for a multifaceted wound dressing offering both antibacterial and antioxidant benefits.

Biofilms of MRSA are intricate structures made up of extracellular polymers such as polysaccharides, proteins, and nucleic acids [54]. These structures serve as a barrier, shielding the bacteria from immune responses and making them less susceptible to antibiotics. To assess their vulnerability to various treatments, we conducted a crystal violet staining test and measured the relative biomass of MRSA biofilms (Fig. 5B–C). The most substantial biofilm disruption was observed in samples treated with both ISD3 hydrogel and NIR. Fig. 5B reveals that ISD3 hydrogel alone managed to limit biofilm development to a degree, but its efficacy was markedly enhanced with the aid of NIR, leading to the formation of a sparse and thin biofilm. These observations were corroborated by three-dimensional confocal laser scanning microscopy analyses (Fig. 5D), where minimal biofilm signals were detected in samples treated with ISD3 and NIR. Conversely, treatment groups involving PBS, ISD1, and ISD1 + NIR showed negligible inhibition of biofilm formation. These findings support the notion that ISD3 hydrogels, when activated photothermally, display strong bactericidal and anti-biofilm properties. Such capabilities establish a strong foundation for their use in treating pressure ulcers compromised by antibiotic-resistant bacterial infections.

3.7. In vitro anti-inflammatory properties of ISD3 hydrogel

After the loaded IAA was released and oxidized to generate ROS to kill bacteria, we hypothesized that functional components in ISD3 hydrogels (such as polyphenol groups derived from dopamine and Pt peroxidase) could further exhibit anti-inflammatory properties by neutralizing inflammatory factors or exerting antioxidant properties. In order to verify our hypothesis, firstly, the cell-level antioxidant capabilities of ISD3 hydrogel were confirmed. Fig. 6A–B indicate that oxidative damage severely curtailed cell proliferation following treatment with hydrogen peroxide (H_2O_2). Contrarily, both groups that received hydrogel treatment showed a marked improvement in cell viability. Specifically, the survival rate in the ISD3 group was notably high: 83.9 % for macrophages and 80.4 % for RS1 cells. To further validate its efficacy, experiments involving oxygen free radical (PTIO), nitrogen free radical (DPPH), and superoxide hydrogen ion ($O_2^{\bullet-}$) scavenging were conducted, which further substantiated the superior ROS scavenging capabilities of the ISD3 hydrogel, as illustrated in Fig. S19.

To delve deeper into assessing the protective effects of the ISD3 hydrogel against oxidative stress, we examined intracellular levels of ROS using a DCFH-DA fluorescent probe [55]. Flow cytometry data (Fig. 6C–D) showed an increase in fluorescence intensity in RAW 264.7 and RS1 cells upon H_2O_2 exposure, indicating elevated ROS levels. In contrast, the set treated with ISD3 hydrogels presented a significant reduction in fluorescence intensity, indicating a decrease in ROS levels. Confocal fluorescence imaging (Fig. 6E–S20 and S21) supported these findings, with the H_2O_2-treated set displaying more pronounced green fluorescence compared to the hydrogel-treated set, where fluorescence was less intense. Such results further substantiate the superior antioxidant capacity of the ISD hydrogel enhanced with IZPP nanoparticles, underscoring its potential efficacy for wound healing applications.

3.8. In vivo pressure ulcer wound healing of ISD3 hydrogel

To investigate the in vivo effectiveness of the proposed ISD3 for expediting the healing of pressure ulcers, a mouse model infected with bacteria was established (Fig. 7A). Initially, the photothermal properties of the ISD hydrogels were evaluated upon application to mouse wounds (Figs. S22 and S23). Upon subjecting the variously treated wounds to 808 nm NIR laser illumination for 3 min, we observed that temperatures in the PBS and ISD1 groups remained stable. In the case of the ISD3 group, the temperature at the wound site escalated to 42.3 °C following 1.5 min of laser exposure and further increased to 49.6 °C after 3 min, affirming previous findings from photothermal performance evaluations. To avoid potential harm to normal tissues due to excessive heat, laser exposure was limited to 1.5 min in subsequent pressure ulcer studies, ensuring the wound's temperature remained around 42 °C.

To assess the hydrogel's blood-clotting capabilities, a murine liver and tail hemostasis model was employed. Given the liver's rich vascularization, injuries resulting in hemorrhage can be particularly difficult to manage through mere vessel constriction [56]. Thus, this model offers an accurate measure of a material's ability to promote blood clotting. In Fig. S24A, treatments involving ISD3 hydrogel demonstrated a significantly enhanced hemostatic impact, showing minimal visible bleeding compared to the evident hemorrhaging in different groups. Such findings were corroborated by the tail hemostasis model (Fig. S24B), which further validated the exceptional ability of ISD3 hydrogel to halt bleeding in vivo.

Following this, our investigation focused on the healing effects of the formulated ISD3 on pressure ulcers in mice. For our negative control, we utilized PBS, while the widely used 3M hydrogel served as our positive control. The experimental groups received either ISD1 or ISD3 hydrogel treatments, with a subset of the ISD3 group also exposed to NIR laser. Photographs were taken to document wounds on days 0, 3, 7, and 14 (Fig. 7B–C). By the third day, both the ISD3 and (ISD3 + NIR)-treated wounds showed a marked reduction in size, especially when compared to the PBS, 3M, and ISD1-treated counterparts. By the seventh day, the (ISD3 + NIR)-treated wound was about 38.1 % less expansive than the one treated with PBS (Fig. 7D). By the 14th day, the PBS, 3M, and ISD1-treated wounds were still considerably vast, covering 35.7 %, 33.4 %, and 23.4 % of the original area. In contrast, the ISD3 treatment shrunk the wound to 14.3 % of its initial size, while in the ISD3 + NIR group, it was a mere 9.5 %. We also gathered bacterial samples from the pressure ulcer wound sites and quantified them using an agar plate technique (Fig. 7E). Consistent with our earlier findings, the PBS, 3M, and ISD1 groups had visible bacterial colonies. Nonetheless, such colonies were less prevalent in the ISD3 set and virtually absent in the ISD3 + NIR set. These results underscore that, particularly when combined with NIR light, the ISD3 hydrogel boasts potent photothermal antibacterial attributes.

Furthermore, two weeks after the surgical procedure, wounds were collected for histological analysis to delve into the ISD3 hydrogel's effect on wound repair. According to the H&E staining outcomes (Fig. 7F), the wound exposed to ISD3 + NIR treatment exhibited the most comprehensive healing, featuring densely packed granulation tissue alongside a fully restored epidermis [57]. On the other hand, the PBS, 3M, and ISD1 groups showed scabs containing infiltrated inflammatory cells. For the ISD3-treated wounds, the granulation tissue appeared underdeveloped, and the epidermis had not fully regenerated [58]. Findings from Masson's trichrome staining (Fig. 7G) demonstrated that in the ISD3 + NIR treatment group, collagen fibers were in line with hair follicles and displayed the most organized arrangement. Besides, TNF-α, a crucial cytokine in immune responses, showed the highest expression in the PBS group, while its levels progressively declined in the 3M, ISD1, ISD3, and ISD3 + NIR groups, implying reduced inflammation due to the ISD3 + NIR treatment (Fig. 7H and S25). CD31, a vascular endothelial cell biomarker, showed limited expression in the negative control group as per immunofluorescence staining. However, its expression significantly increased in the ISD3-treated group and was highest in the (ISD3 + NIR)-treated wounds, signaling optimal new blood vessel formation in the regenerated skin tissues (Fig. 7I and S26).

Simultaneously, our study focused on the function of macrophages in healing pressure ulcer wounds. These cells are vital in the immune

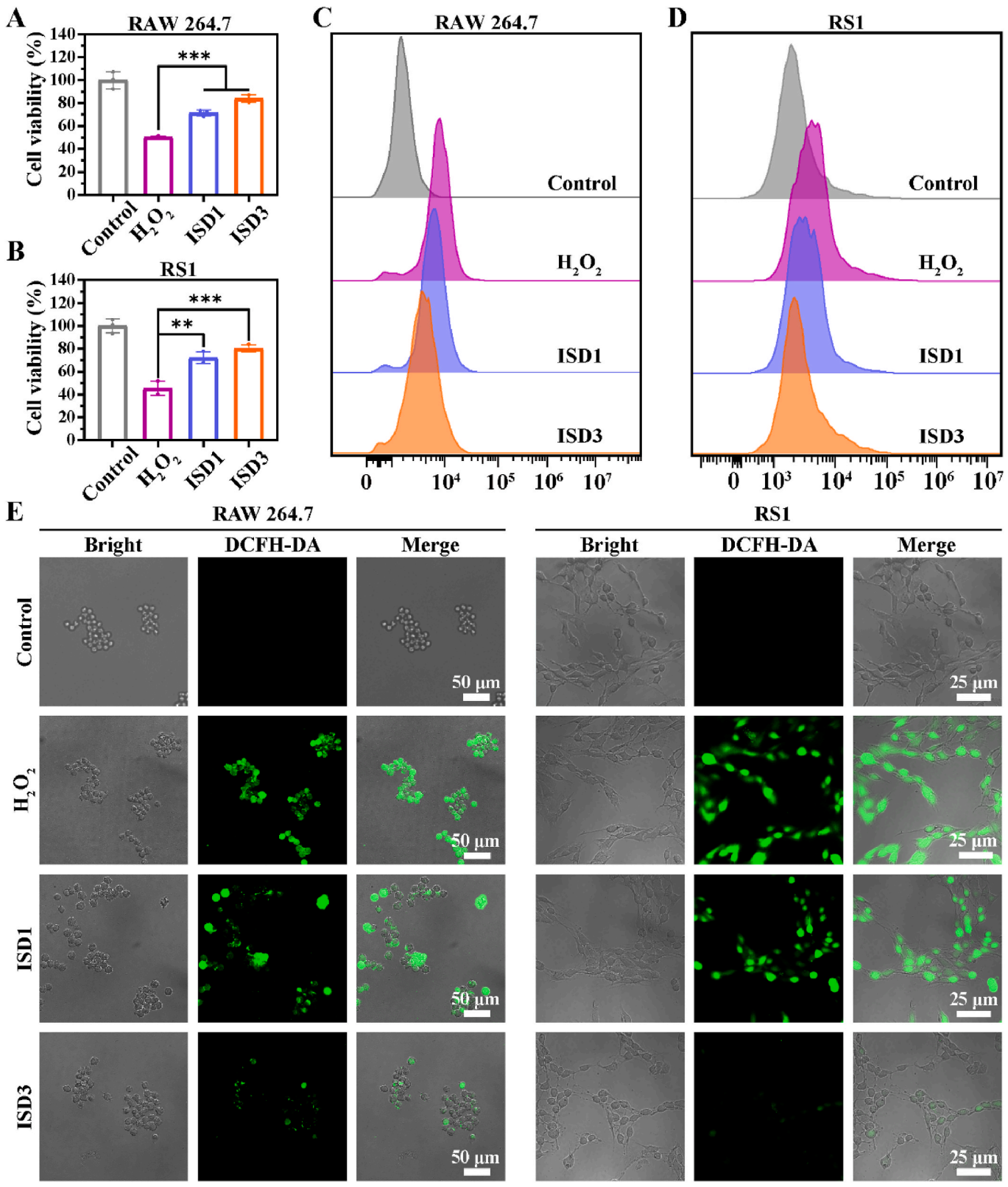

Fig. 6. In vitro cellular assessments of ISD3 hydrogel. (A and B) Cytotoxic consequences on RAW 264.7 cells (A) and RS1 cells (B) after exposure to ISD hydrogel and H_2O_2. (C and D) Analysis of ROS levels within RAW 264.7 cells (C) and RS1 cells (D) via flow cytometry, using DCFH-DA as the marker. (E) Typical white-light and fluorescence images displaying intracellular ROS in RAW 264.7 cells (left) and RS1 cells (right) after oxidative stress pre-treatment. Error bars represent the mean ± SD (n = 6). Symbols *** and ** denote $P < 0.001$ and $P < 0.01$.

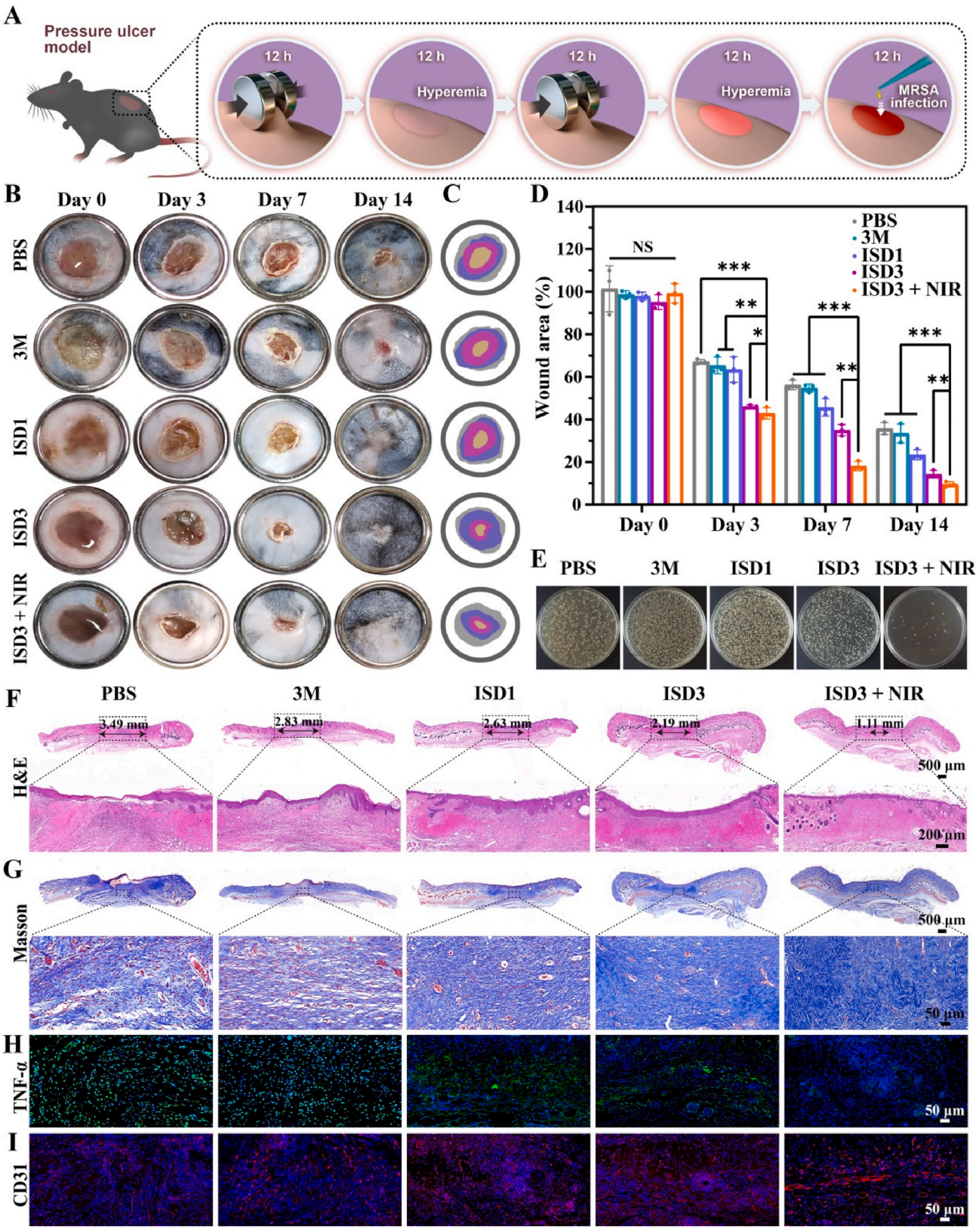

Fig. 7. Evaluating the effectiveness of ISD3 hydrogel in mouse pressure ulcer treatment. (A) Diagram illustrating the model of pressure ulcers with bacterial infections. (B) Sequential digital images showing skin lesions across PBS, 3M, ISD1, ISD3, and ISD3 + NIR groups over two weeks. (C) Visual representation of wound healing on days 0, 3, 7, and 14. (D) Measurement of wound dimensions for each examined set. (E) Captured images of bacterial colonies from the wound site following various treatments displayed on agar plates. (F–I) Histological staining of mouse dermal tissue within the lesion area: H&E for (F), Masson for (G), TNF-α for (H), and CD31 for (I). Error bars show mean ± SD (n = 6). Statistical significance levels are denoted as follows: *** for $P < 0.001$, ** for $P < 0.01$, * for $P < 0.05$, and NS for $P > 0.05$.

response following tissue injury. They shift from a pro-inflammatory state (M1) to an anti-inflammatory one (M2), impacting tissue repair adversely. Immunofluorescence staining was instrumental in this research: CD86 identified pro-inflammation M1 macrophages, while CD206 marked anti-inflammation M2 macrophages. Fig. S27A reveals that CD86 levels were significantly reduced in samples treated with hydrogel relative to the control group. Conversely, the average fluorescence intensity of CD206 experienced a rise in samples treated with ISD3 hydrogel (Fig. S27B). Notably, in the ISD3 + NIR group, CD86-positive cell counts were substantially lower than in other groups, while CD206 expression was the highest (Figs. S28 and S29). These findings suggest that ISD3 + NIR facilitates a swift shift in macrophage phenotype from M1 to M2. This transition assists in diminishing inflammatory responses, boosting angiogenesis and remodeling skin tissue, ultimately facilitating quick and high-quality recovery from pressure ulcer wounds [59]. Besides, Fig. S30 illustrates the impact of various treatments on the organs of the mouse. H&E staining verified that neither the hydrogel nor NIR treatment resulted in detrimental alterations to the tissues. These findings illustrate that the ISD3 hydrogel, particularly when augmented with NIR, can both hasten epidermal restoration and mitigate inflammation, offering a new methodology for pressure ulcer wound management.

3.9. Analyzing the therapeutic efficacy of ISD3 hydrogel through RNA sequencing

To further delve into the intrinsic mechanisms of wound healing associated with ISD3 hydrogel, transcriptome sequencing was conducted. Protein expression disparities among the groups were evident in Fig. 8A, as delineated by principal component analysis (PCA). Fig. 8B reveals varied gene expression in cells treated with ISD3 versus the control, delineated in a volcano plot; genes with high activity are highlighted in red, while those less active appear in blue. Subsequently, an assessment of differentially expressed genes (DEGs) in cells pinpointed those participating in the healing process, focusing on the antioxidant impacts of medicinal treatments. In total, 75 DEGs were implicated in the antioxidative healing stages (Fig. 8E). The GSEA plot illustrates that, compared to the control group, the ISD3 cohort markedly suppressed peroxidase expression, underscoring the substantial role of ISD3 hydrogel in curtailing oxidative stress (Fig. 8C) [60].

Subsequently, genes differentially expressed and linked to the peroxisome signaling pathway were pinpointed, as depicted in Fig. 8D. Over thirty proteins, known as Pex proteins, are recognized for their involvement in the creation of peroxisomes—common organelles that play roles in lipid and ROS metabolism. The family of homologous proteins, Pex11, is known to facilitate the division and multiplication of peroxisomes. In summary, outcomes from transcriptome sequencing indicate that the activated Pex11 protein is instrumental in boosting the antioxidant and inflammatory responses mediated by ISD3 hydrogel [61].

Next, selected DEGs (P value < 0.05, FC > 1.2) underwent further analysis for over-representation. Proteins showing decreased expression, tagged with their respective gene names, were linked to lower inflammation markers (e.g., FOS, TNF, EFNA4, DUSP9, and JUN). Conversely, proteins with increased expression correlated with the growth, formation, and expansion of blood vessels (e.g., ROBO4, CXCL8, JAG1, UNC58, PANK2, and EREG), as shown in Fig. 8F–G [62]. To delve deeper into the anti-inflammation properties of ISD3, we conducted Gene Ontology (GO) and Kyoto Encyclopedia of Genes and Genomes (KEGG) analyses. The GO database categorizes genes and their products, focusing on their roles in angiogenesis, enhancing cell adhesion, and constructing the extracellular matrix (Fig. 8H). KEGG annotations and enrichment assessments revealed that miRNA target genes primarily function in the MAPK pathway (Fig. 8I). The p38 MAPK signaling pathway is crucial in managing stress reactions, including inflammation and cellular apoptosis. Additionally, increased endogenous oxidative stress in aging tissues can trigger senescence signals mediated by p38 MAPK. Consequently, ISD3 that possesses ATP-activated ROS generation and further ROS scavenging plays a role in mitigating inflammation by targeting and modulating the MAPK signaling pathway, ultimately achieving accelerated healing of pressure ulcers.

Together, we proposed an ATP-activated prodrug strategy for generating ROS to treat pressure ulcers infected with MDR bacteria. This approach is distinguished and advantageous due to the following features:

(1) ATP-Triggered Activation: The prodrug system is triggered by ATP secreted by bacteria, creating a clear distinction between infected and healthy tissues. Healthy cells do not release ATP in concentrations sufficient to cause the disassembly of the ZIF-8 carrier. As a result, ROS production mainly occurs in environments with bacterial presence and elevated ATP levels, ensuring that ROS generation is localized at the infection site and minimizing potential damage to nearby healthy cells.
(2) Spatiotemporal Control of ROS Generation: The system employs 808 nm NIR light to boost ROS generation by catalyzing the IAA prodrug in the presence of PDA@Pt nanoparticles. The duration, intensity, and frequency of NIR light exposure can be precisely adjusted to limit both the photothermal effect and ROS production to levels effective for eliminating bacteria while protecting surrounding tissues. After achieving optimal antibacterial efficacy, the system shifts to a dormant state, stopping further ROS generation. This mechanism effectively prevents prolonged ROS production, which could otherwise harm healthy cells and tissues during the later stages of healing.
(3) Physical Isolation and Controlled Release: The nanoparticles' core-shell architecture effectively separates the prodrug (IAA) from the catalytic agent (PDA@Pt), thereby avoiding premature activation of ROS. This encapsulation guarantees that ROS generation occurs exclusively when bacterial ATP disrupts the ZIF-8 framework in a precisely timed and localized manner. Such a targeted strategy confines ROS production to areas with bacterial presence, protecting healthy cells that do not produce enough ATP to trigger nanoparticle degradation.
(4) Hydrogel Matrix as a Modulator: SFMA-DA fulfills dual roles by maintaining moisture essential for wound healing and concentrating bacteria within the hydrogel matrix. The interaction between bacteria and the hydrogel increases the local ATP levels, facilitating the reaction between ATP and the components responsible for ROS generation. Consequently, ROS production is focused on regions where bacteria are located. Additionally, the hydrogel supports tissue regeneration by acting as a scaffold and diminishes inflammation, which is especially advantageous during the later phases of wound healing. This balance mitigates the harmful effects of ROS and photothermal treatment while promoting effective tissue repair.
(5) Photothermal Regulation: The photothermal effect was deliberately maintained at a mild hyperthermia level ($<45\ ^{\circ}C$) to protect healthy tissue from damage. Experimental adjustments of NIR exposure and nanoparticle concentrations enabled precise control of temperature increases, ensuring they remained non-damaging to healthy cells. Simultaneously, these adjustments enhanced the antibacterial efficacy of ROS production, achieving effective bacterial elimination without compromising surrounding healthy tissue.

4. Conclusions

To summarize, we developed an ATP-responsive prodrug system (ISD3) that combines IZPP nanoparticles with a SFMA-DA hydrogel matrix for targeted bacterial infection intervention. The crafted IZPP mechanism ensures dual transportation of IAA and PP nanozyme in a

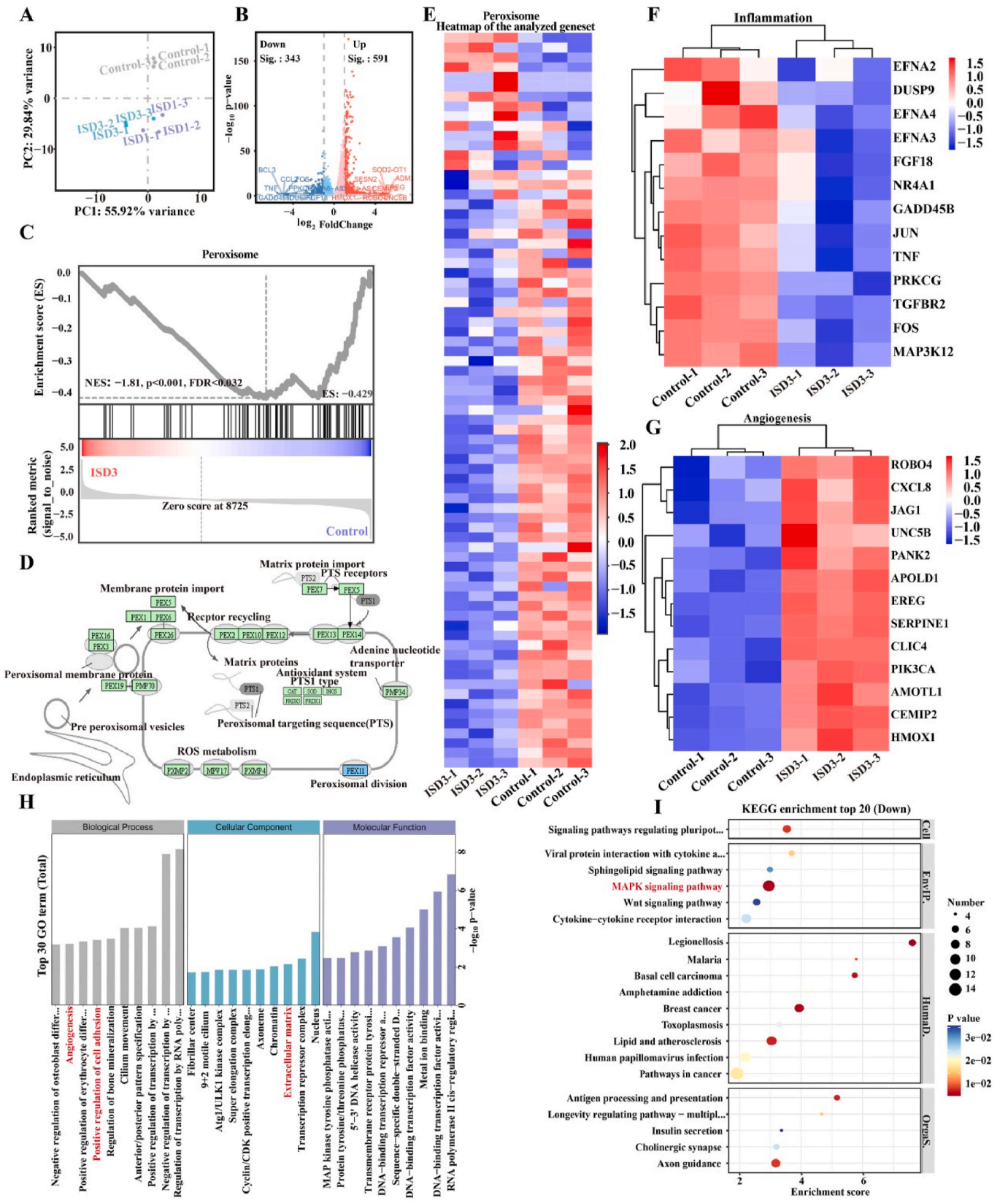

Fig. 8. Profile of mRNA expressions after ISD3 hydrogel treatment detected via RNA-sequencing. (A) PCA demonstrating distinct separation among the groups based on the proteins expressed differently. (B) A volcano plot illustrating proteins expressed differently. (C) GSEA highlighting the DEGs in the peroxisome pathway. (D) Overview of genes expressed differently in response to peroxisome. Green indicates genes active in peroxidase; blue represents genes that are upregulated. (E) A heatmap displaying proteins expressed differently in the peroxisome. (F and G) Heatmaps depicting the comparative gene expression related to inflammation (F) and angiogenesis (G) between the control and ISD3 groups. (H and I) Annotations and enrichment analysis by GO (H) and KEGG (I) for miRNA target genes.

singular carrier while keeping the pre-encapsulated IAA separate from the Pt, thus averting early activation and undesired ROS creation. To bolster its retention and stability, the IZPP is encased within the SFMA-DA hydrogel. Upon administering ISD3 to regions infected by MDR bacteria, IZPP's structure responds to ATP released by these microbes, which enables the simultaneous and spatial convergence of IAA prodrug and PP nanozyme on a unified carrier, thus effectively producing ROS. Catalytic efficiency is enhanced when exposed to 808 nm near-infrared light, causing an increase in ROS levels sufficient for efficient bacterial elimination. Following the confirmation of significant antibacterial impact, the complete hybrid ISD3 system enters a dormant phase, ceasing further ROS production. Additionally, elements like polyphenols in the ISD3 hydrogel work to neutralize substances that cause inflammation in chronic pressure ulcer wounds, aiding in their healing. To conclude, our study introduces an ATP-responsive inorganic-organic hydrogel prodrug system skilled at precisely controlling ROS production, thereby hastening the healing process of MDR bacteria-infected pressure ulcers. Our developed ISD3 approach offers a strong solution to the difficulties linked with concurrent transport and premature activation, commonly encountered in conventional prodrug systems.

CRediT authorship contribution statement

Xiaoliang Qi: Writing – original draft, Methodology, Investigation. **Yajing Xiang:** Software. **Ying Li:** Methodology. **Jiajia Wang:** Data curation. **Yuxi Chen:** Data curation. **Yulong Lan:** Data curation. **Jinsong Liu:** Visualization. **Jianliang Shen:** Supervision.

Author information

All authors have approved the final version of this manuscript.

Ethics approval and consent to participate

Animal research was performed in strict adherence to the guidelines set by the Animal Ethics Committee of Wenzhou Medical University, which approved the authorization number xmsq2022-0238.

Declaration of interests statement

Jianliang Shen is an editorial board member for Bioactive Materials and was not involved in the editorial review or the decision to publish this article. All authors declare that there are no competing interests.

Acknowledgements

This work was financially supported by the Zhejiang Provincial Natural Science Foundation for Distinguished Young Scholar (LR23C100001) and the National Natural Science Foundation of China (21977081).

Appendix A. Supplementary data

Supplementary data to this article can be found online at https://doi.org/10.1016/j.bioactmat.2024.11.029.

References

[1] J. Shan, X. Li, Z. Huang, B. Kong, H. Wang, L. Ren, In situ sprayed difunctional gel avoiding microenvironments limitations to treat pressure ulcers, Macromol. Biosci. 23 (5) (2023) 2300006.
[2] L. Luo, H. Zhang, S. Zhang, C. Luo, X. Kan, J. Lv, P. Zhao, Z. Tian, C. Li, Extracellular vesicle-derived silk fibroin nanoparticles loaded with MFGE8 accelerate skin ulcer healing by targeting the vascular endothelial cells, J. Nanobiotechnol. 21 (1) (2023) 455.
[3] V. Falanga, R.R. Isseroff, A.M. Soulika, M. Romanelli, D. Margolis, S. Kapp, M. Granick, K. Harding, Chronic wounds, Nat. Rev. Dis. Prim. 8 (1) (2022) 50.
[4] W. Qiu, Q. Wang, M. Li, N. Li, X. Wang, J. Yu, F. Li, D. Wu, 3D hybrid scaffold with aligned nanofiber yarns embedded in injectable hydrogels for monitoring and repairing chronic wounds, Comp. Part B 234 (2022) 109688.
[5] Z. Peng, T.T. Nguyen, M. Wang, B. Anderson, M.M. Konai, V.A. Schroeder, W. R. Wolter, T. Page-Mayberry, C.E. Peterson, S. Mobashery, M. Chang, Proteomics identification of targets for intervention in pressure ulcers, ACS Chem. Biol. 17 (6) (2022) 1357–1363.
[6] A. Gefen, Alternatives and preferences for materials in use for pressure ulcer prevention: an experiment-reinforced literature review, Int. Wound J. 19 (7) (2022) 1797–1809.
[7] A. Grigatti, A. Gefen, What makes a hydrogel-based dressing advantageous for the prevention of medical device-related pressure ulcers, Int. Wound J. 19 (3) (2022) 515–530.
[8] R. Toita, E. Shimizu, M. Murata, J.-H. Kang, Protective and healing effects of apoptotic mimic-induced M2-like macrophage polarization on pressure ulcers in young and middle-aged mice, J. Contr. Release 330 (2021) 705–714.
[9] A. Zhang, H. Wu, X. Chen, Z. Chen, Y. Pan, W. Qu, H. Hao, D. Chen, S. Xie, Targeting and arginine-driven synergizing photodynamic therapy with nutritional immunotherapy nanosystems for combating MRSA biofilms, Sci. Adv. 9 (28) (2023) eadg9116.
[10] D. Pranantyo, C.K. Yeo, Y. Wu, C. Fan, X. Xu, Y.S. Yip, M.I.G. Vos, S. H. Mahadevegowda, P.L.K. Lim, L. Yang, P.T. Hammond, D.I. Leavesley, N.S. Tan, M.B. Chan-Park, Hydrogel dressings with intrinsic antibiofilm and antioxidative dual functionalities accelerate infected diabetic wound healing, Nat. Commun. 15 (1) (2024) 954.
[11] X. Wang, Q. Li, Y. Miao, X. Chen, X. Zhang, J. Shi, F. Liu, X. Wang, Z. Li, Y. Yang, X. Zhang, J. Wang, J. Duan, A 0D-2D heterojunction bismuth molybdate-anchored multifunctional hydrogel for highly efficient eradication of drug-resistant bacteria, ACS Nano 17 (16) (2023) 15568–15589.
[12] Y. Xiang, J. Lu, C. Mao, Y. Zhu, C. Wang, J. Wu, X. Liu, S. Wu, K.Y.H. Kwan, K.M. C. Cheung, K.W.K. Yeung, Ultrasound-triggered interfacial engineering-based microneedle for bacterial infection acne treatment, Sci. Adv. 9 (10) (2023) eadf0854.
[13] C. Feng, J. Ouyang, Z. Tang, N. Kong, Y. Liu, L. Fu, X. Ji, T. Xie, O.C. Farokhzad, W. Tao, Germanene-based theranostic materials for surgical adjuvant treatment: inhibiting tumor recurrence and wound infection, Matter 3 (1) (2020) 127–144.
[14] L. Yang, D. Zhang, W. Li, H. Lin, C. Ding, Q. Liu, L. Wang, Z. Li, L. Mei, H. Chen, Y. Zhao, X. Zeng, Biofilm microenvironment triggered self-enhancing photodynamic immunomodulatory microneedle for diabetic wound therapy, Nat. Commun. 14 (1) (2023) 7658.
[15] Y. Xu, Y. Luo, Z. Weng, H. Xu, W. Zhang, Q. Li, H. Liu, L. Liu, Y. Wang, X. Liu, L. Liao, X. Wang, Microenvironment-responsive metal-phenolic nanozyme release platform with antibacterial, ROS scavenging, and osteogenesis for periodontitis, ACS Nano 17 (19) (2023) 18732–18746.
[16] H. Wu, F. Li, W. Shao, J. Gao, D. Ling, Promoting angiogenesis in oxidative diabetic wound microenvironment using a nanozyme-reinforced self-protecting hydrogel, ACS Cent. Sci. 5 (3) (2019) 477–485.
[17] X. Qi, Y. Xiang, E. Cai, S. You, T. Gao, Y. Lan, H. Deng, Z. Li, R. Hu, J. Shen, All-in-one: harnessing multifunctional injectable natural hydrogels for ordered therapy of bacteria-infected diabetic wounds, Chem. Eng. J. 439 (2022) 135691.
[18] X. He, J.T. Hou, X. Sun, P. Jangili, J. An, Y. Qian, J.S. Kim, J. Shen, NIR-II photo-amplified sonodynamic therapy using sodium molybdenum bronze nanoplatform against subcutaneous *Staphylococcus aureus* infection, Adv. Funct. Mater. 32 (38) (2022) 202203964.
[19] Y. Weng, H. Chen, X. Chen, H. Yang, C.H. Chen, H. Tan, Adenosine triphosphate-activated prodrug system for on-demand bacterial inactivation and wound disinfection, Nat. Commun. 13 (1) (2022) 4712.
[20] X. Yu, X. Fu, J. Yang, L. Chen, F. Leng, Z. Yang, C. Yu, Glucose/ROS cascade-responsive ceria nanozymes for diabetic wound healing, Mater. Today Bio 15 (2022) 100308.
[21] E. Cai, X. Qi, Y. Shi, X. Ge, Y. Xiang, H. Xu, Y. Li, Y. Lan, J. Shen, R. Hu, H. Deng, Immunomodulatory melanin@Pt nanoparticle-reinforced adhesive hydrogels for healing diabetic oral ulcers, Chem. Eng. J. 488 (2024) 150372.
[22] X. Qi, Y. Shi, C. Zhang, E. Cai, X. Ge, Y. Xiang, Y. Li, B. Zeng, J. Shen, A hybrid hydrogel with intrinsic immunomodulatory functionality for treating multidrug-resistant Pseudomonas aeruginosa infected diabetic foot ulcers, ACS Mater. Lett. 6 (7) (2024) 2533–2547.
[23] M. Kim, R. Xin, J. Earnshaw, J. Tang, J.P. Hill, A. Ashok, A.K. Nanjundan, J. Kim, C. Young, Y. Sugahara, J. Na, Y. Yamauchi, MOF-derived nanoporous carbons with diverse tunable nanoarchitectures, Nat. Protoc. 17 (12) (2022) 2990–3027.
[24] Z. Yuan, J. Wu, Z. Fu, S. Meng, L. Dai, K. Cai, Polydopamine-mediated interfacial functionalization of implants for accelerating infected bone repair through light-activatable antibiosis and carbon monoxide gas regulated macrophage polarization, Adv. Funct. Mater. 32 (27) (2022) 2200374.
[25] W.-L. Liu, T. Liu, A.M. Cao, S.-Y. Qin, J. Feng, X.-Z. Zhang, Coordination between anti-inflammation and antitumor actions for systematic tumor treatments with improved prognosis, Chem. Eng. J. 439 (2022) 135711.
[26] W. Dai, L. Zhang, Y. Yu, W. Yan, F. Zhao, Y. Fan, C. Cao, Q. Cai, X. Hu, Y. Ao, 3D bioprinting of heterogeneous constructs providing tissue-specific microenvironment based on host–guest modulated dynamic hydrogel bioink for osteochondral regeneration, Adv. Funct. Mater. 32 (23) (2022) 2200710.
[27] X. He, X. Liao, H. Li, W. Xia, H. Sun, Bismuth-induced inactivation of ferric uptake regulator from Helicobacter pylori, Inorg. Chem. 56 (24) (2017) 15041–15048.
[28] C. Zhang, E. Cai, X. Qi, X. Ge, Y. Xiang, J. Wang, Y. Li, L. Lv, H. Zheng, Y. Qian, W. Dong, H. Li, J. Shen, Immunomodulatory gallium/glycyrrhizic acid hydrogels

for treating multidrug-resistant Pseudomonas aeruginosa-infected pressure ulcers, Chem. Eng. J. 487 (2024) 150756.
[29] Q. Zeng, Y. Qian, Y. Huang, F. Ding, X. Qi, J. Shen, Polydopamine nanoparticle-dotted food gum hydrogel with excellent antibacterial activity and rapid shape adaptability for accelerated bacteria-infected wound healing, Bioact. Mater. 6 (9) (2021) 2647–2657.
[30] X. He, H. Chen, C. Xu, J. Fan, W. Xu, Y. Li, H. Deng, J. Shen, Ratiometric and colorimetric fluorescent probe for hypochlorite monitor and application for bioimaging in living cells, bacteria and zebrafish, J. Hazard Mater. 388 (2020) 122029.
[31] F. Zhang, Y. Kang, L. Feng, G. Xi, W. Chen, N. Kong, W. Tao, T. Luan, S. Koo, X. Ji, Infected wound repair with an ultrasound-enhanced nanozyme hydrogel scaffold, Mater. Horiz. 10 (12) (2023) 5474–5483.
[32] Q. Liang, J. Xi, X.J. Gao, R. Zhang, Y. Yang, X. Gao, X. Yan, L. Gao, K. Fan, A metal-free nanozyme-activated prodrug strategy for targeted tumor catalytic therapy, Nano Today 35 (2020) 100935.
[33] X. Qi, Y. Xiang, E. Cai, X. Ge, X. Chen, W. Zhang, Z. Li, J. Shen, Inorganic–organic hybrid nanomaterials for photothermal antibacterial therapy, Coord. Chem. Rev. 496 (2023) 215426.
[34] L. Lin, L. Xu, W. Sun, L. Liang, X. Qi, Y.E. Zhao, Mild photothermal therapy prevents posterior capsule opacification through cytoskeletal remodeling, Adv. Healthcare Mater. 12 (29) (2023) 2300470.
[35] Y. Kang, N. Kong, M. Ou, Y. Wang, Q. Xiao, L. Mei, B. Liu, L. Chen, X. Zeng, X. Ji, A novel cascaded energy conversion system inducing efficient and precise cancer therapy, Bioact. Mater. 20 (2023) 663–676.
[36] W. Zhu, Y. Dong, P. Xu, Q. Pan, K. Jia, P. Jin, M. Zhou, Y. Xu, R. Guo, B. Cheng, A composite hydrogel containing resveratrol-laden nanoparticles and platelet-derived extracellular vesicles promotes wound healing in diabetic mice, Acta Biomater. 154 (2022) 212–230.
[37] J. Gong, C. Ye, J. Ran, X. Xiong, X. Fang, X. Zhou, Y. Yi, X. Lu, J. Wang, C. Xie, J. Liu, Polydopamine-mediated immunomodulatory patch for diabetic periodontal tissue regeneration assisted by metformin-ZIF system, ACS Nano 17 (17) (2023) 16573–16586.
[38] X. Qi, T. Su, M. Zhang, X. Tong, W. Pan, Q. Zeng, J. Shen, Sustainable, flexible and biocompatible hydrogels derived from microbial polysaccharides with tailorable structures for tissue engineering, Carbohydr. Polym. 237 (2020) 116160.
[39] Y. Song, Y. You, X. Xu, J. Lu, X. Huang, J. Zhang, L. Zhu, J. Hu, X. Wu, X. Xu, W. Tan, Y. Du, Adipose-derived mesenchymal stem cell-derived exosomes biopotentiated extracellular matrix hydrogels accelerate diabetic wound healing and skin regeneration, Adv. Sci. 10 (30) (2023) 2304023.
[40] G. Wang, X. Meng, P. Wang, X. Wang, G. Liu, D.A. Wang, C. Fan, A catechol bioadhesive for rapid hemostasis and healing of traumatic internal organs and major arteries, Biomaterials 291 (2022) 121908.
[41] W. Zhang, B. Wang, G. Xiang, T. Jiang, X. Zhao, Photodynamic alginate Zn-mof thermosensitive hydrogel for accelerated healing of infected wounds, ACS Appl. Mater. Interfaces 15 (19) (2023) 22830–22842.
[42] X. Qi, E. Cai, Y. Xiang, C. Zhang, X. Ge, J. Wang, Y. Lan, H. Xu, R. Hu, J. Shen, An immunomodulatory hydrogel by hyperthermia-assisted self-cascade glucose depletion and ROS scavenging for diabetic foot ulcer wound therapeutics, Adv. Mater. 35 (48) (2023) 2306632.
[43] Y. Xiang, X. Qi, E. Cai, C. Zhang, J. Wang, Y. Lan, H. Deng, J. Shen, R. Hu, Highly efficient bacteria-infected diabetic wound healing employing a melanin-reinforced biopolymer hydrogel, Chem. Eng. J. 460 (2023) 141852.
[44] J. Zheng, R. Fan, H. Wu, H. Yao, Y. Yan, J. Liu, L. Ran, Z. Sun, L. Yi, L. Dang, P. Gan, P. Zheng, T. Yang, Y. Zhang, T. Tang, Y. Wang, Directed self-assembly of herbal small molecules into sustained release hydrogels for treating neural inflammation, Nat. Commun. 10 (1) (2019) 1604.
[45] Z. Shao, T. Yin, J. Jiang, Y. He, T. Xiang, S. Zhou, Wound microenvironment self-adaptive hydrogel with efficient angiogenesis for promoting diabetic wound healing, Bioact. Mater. 20 (2023) 561–573.
[46] T. Su, M. Zhang, Q. Zeng, W. Pan, Y. Huang, Y. Qian, W. Dong, X. Qi, J. Shen, Mussel-inspired agarose hydrogel scaffolds for skin tissue engineering, Bioact. Mater. 6 (3) (2021) 579–588.
[47] X. Ji, Z. Tang, H. Liu, Y. Kang, L. Chen, J. Dong, W. Chen, N. Kong, W. Tao, T. Xie, Nanoheterojunction-mediated thermoelectric strategy for cancer surgical adjuvant treatment and beta-elemene combination therapy, Adv. Mater. 35 (8) (2023) 2207391.
[48] Y. Wang, L. Sun, G. Chen, H. Chen, Y. Zhao, Structural color ionic hydrogel patches for wound management, ACS Nano 17 (2) (2022) 1437–1447.
[49] X. He, L. Dai, L. Ye, X. Sun, O. Enoch, R. Hu, X. Zan, F. Lin, J. Shen, A vehicle-free antimicrobial polymer hybrid gold nanoparticle as synergistically therapeutic platforms for *Staphylococcus aureus* infected wound healing, Adv. Sci. 9 (14) (2022) 2105223.
[50] X. He, Y. Lv, Y. Lin, H. Yu, Y. Zhang, Y. Tong, C. Zhang, Platinum nanoparticles regulated V_2C MXene nanoplatforms with NIR-II enhanced nanozyme effect for photothermal and chemodynamic anti-infective therapy, Adv. Mater. 36 (25) (2024) 2400366.
[51] Z. Li, D. Xu, Z. Deng, J. Yin, Y. Qian, J.-T. Hou, X. Ding, J. Shen, X. He, Single-Atom-Catalyzed MXene-Based nanoplatform with Photo-Enhanced Peroxidase-Like activity nanotherapeutics for *Staphylococcus aureus* infection, Chem. Eng. J. 452 (2023) 139587.
[52] X. He, E. Obeng, X. Sun, N. Kwon, J. Shen, J. Yoon, Polydopamine, harness of the antibacterial potentials-A review, Mater. Today Bio 15 (2022) 100329.
[53] P. Wu, W. Zuo, Y. Wang, Q. Yuan, J. Yang, X. Liu, H. Jiang, J. Dai, F. Xue, Y. Ju, Multimodal capture – antibody-independent lateral flow immunoassay based on AuNF – PMBA for point-of-care diagnosis of bacterial urinary tract infections, Chem. Eng. J. 451 (2023) 139021.
[54] X. He, S. Koo, E. Obeng, A. Sharma, J. Shen, J.S. Kim, Emerging 2D MXenes for antibacterial applications: current status, challenges, and prospects, Coord. Chem. Rev. 492 (2023) 215275.
[55] Y. Kang, L. Xu, J. Dong, X. Yuan, J. Ye, Y. Fan, B. Liu, J. Xie, X. Ji, Programmed microalgae-gel promotes chronic wound healing in diabetes, Nat. Commun. 15 (1) (2024) 1042.
[56] Y. Zhao, C. Tian, Y. Liu, Z. Liu, J. Li, Z. Wang, X. Han, All-in-one bioactive properties of photothermal nanofibers for accelerating diabetic wound healing, Biomaterials 295 (2023) 122029.
[57] Y. Fan, P. Yang, H. Ma, Y. Liu, X. Ding, Y. Hu, G. Cheng, F.-J. Xu, One ternary nucleic acid delivery system with smart dextran-peptide coating enables in vivo and ex vivo wound therapy, Matter 6 (1) (2023) 239–259.
[58] X. Qi, X. Ge, X. Chen, E. Cai, Y. Xiang, H. Xu, Y. Li, Y. Lan, Y. Shi, H. Deng, J. Shen, An immunoregulation hydrogel with controlled hyperthermia-augmented oxygenation and ROS scavenging for treating diabetic foot ulcers, Adv. Funct. Mater. 34 (33) (2024) 2400489.
[59] J. Ye, Y. Fan, Y. She, J. Shi, Y. Yang, X. Yuan, R. Li, J. Han, L. Liu, Y. Kang, X. Ji, Biomimetic self-propelled asymmetric nanomotors for cascade-targeted treatment of neurological inflammation, Adv. Sci. 11 (22) (2024) 2310211.
[60] Y. Xiang, Z. Pan, X. Qi, X. Ge, J. Xiang, H. Xu, E. Cai, Y. Lan, X. Chen, Y. Li, Y. Shi, J. Shen, J. Liu, A cuttlefish ink nanoparticle-reinforced biopolymer hydrogel with robust adhesive and immunomodulatory features for treating oral ulcers in diabetes, Bioact. Mater. 39 (2024) 562–581.
[61] S. Mindthoff, S. Grunau, L.L. Steinfort, W. Girzalsky, J.K. Hiltunen, R. Erdmann, V. D. Antonenkov, Peroxisomal Pex11 is a pore-forming protein homologous to TRPM channels, Biochim. Biophys. Acta, Mol. Cell Res. 1863 (2) (2016) 271–283.
[62] Y. Hua, K. Wang, Y. Huo, Y. Zhuang, Y. Wang, W. Fang, Y. Sun, G. Zhou, Q. Fu, W. Cui, K. Zhang, Four-dimensional hydrogel dressing adaptable to the urethral microenvironment for scarless urethral reconstruction, Nat. Commun. 14 (1) (2023) 7632.